THE GEOLOGICAL SOCIETY OF AMERICA®

# Early Paleozoic slab rollback in the North Altun, Northwest China: New evidence from mafic intrusions and high-Mg andesites

**Xian-Tao Ye[1], Chuan-Lin Zhang[1], Ai-Guo Wang[2], Bin Wu[2], and Guo-Dong Wang[3]**

[1]COLLEGE OF OCEANOGRAPHY, HOHAI UNIVERSITY, 1 XIKANG ROAD, NANJING, 210098, CHINA

[2]NANJING CENTER, CHINA GEOLOGICAL SURVEY, 534 EAST ZHONGSHAN ROAD, NANJING, 210016, CHINA

[3]SHANDONG PROVINCIAL KEY LABORATORY OF WATER AND SOIL CONSERVATION AND ENVIRONMENTAL PROTECTION, SCHOOL OF RESOURCE AND ENVIRONMENTAL SCIENCES, LINYI UNIVERSITY, SHUANGLING ROAD, LINYI, 276000, CHINA

## ABSTRACT

North Altun, one of the key tectonic units of the Altun orogen, lies at the northern margin of the Qinhai-Tibet Plateau. This belt is marked by high- to ultrahigh-pressure metamorphic rocks, ophiolites, and granitic rocks. To refine the model of subduction processes in the North Altun, we report detailed studies on the petrography, geochronology, and elemental and isotopic geochemistry of the mafic intrusions and andesitic lavas in the Kaladawan area along the northern margin of the Altun. Zircon U-Pb ages of rhyolites from the Lapeiquan Formation indicate that the Lapeiquan volcanic-sedimentary sequences were deposited in the late Cambrian (485–495 Ma), whereas the Dawan gabbros and Dabanxi mafic intrusions were emplaced at ca. 515 Ma and ca. 460 Ma, respectively. The Dawan gabbros generally produce flat rare earth element (REE) patterns ($[La/Yb]_N$ = 0.99–1.07) and negative Nb anomalies on primitive mantle–normalized diagrams (Nb/La = 0.13–0.80). These gabbros have positive $\varepsilon_{Nd}(t)$ values (+0.6 to +7.4), indicative of a depleted mantle source. These features reveal that the Dawan gabbros were probably derived from asthenospheric mantle with variable involvement of lithospheric mantle. The andesites from the Lapeiquan Formation are characterized by high Mg# (40–58) and $TiO_2$ contents (0.61–1.21 wt%), sharing the signatures of calc-alkaline high-Mg andesites, and they are complemented by light (L) REE enrichment and strong Nb depletion. Their isotopic compositions show negative $\varepsilon_{Nd}(t)$ values (–3.7 to –5.8). Geochemical data indicate that the high-Mg andesites were produced by interaction between sediment-derived melts and mantle wedge peridotite–derived basaltic melts. The slightly younger Dabanxi gabbros display enriched LREE and depleted high field strength element (HFSE) patterns. Isotopically, they have variable positive whole-rock $\varepsilon_{Nd}(t)$ values (+0.6 to +4.1). Integrating the elemental and Nd isotopic compositions, we suggest that the primitive magmas of the Dabanxi gabbroic intrusion were most likely derived from the mantle wedge that was modified by slab-derived fluids.

Combined with previous studies, we conclude that the formation of the Dawan gabbros and Dawan high-Mg andesites in the North Altun was related to asthenospheric upwelling triggered by rollback of the North Altun oceanic slab. We infer that these rocks in the North Altun area might represent part of a previously active arc–back-arc basin system.

LITHOSPHERE; v. 10; no. 6; p. 687–707; GSA Data Repository Item 2018355 | Published online 17 October 2018 https://doi.org/10.1130/L732.1

## INTRODUCTION

The Altun orogen is located at the northern margin of the Qinhai-Tibet Plateau (Fig. 1A; Wu et al., 2006, 2009; Xu et al., 1999, 2011). Recent studies show that the Altun orogen is a composite orogenic belt, consisting of microcontinents and multiple ophiolite and high-pressure to ultrahigh-pressure metamorphic belts (Xu et al., 1999; Zhang et al., 2005b). In spite of many studies in the area, its Paleozoic tectonic evolution has remained equivocal (Cowgill et al., 2003; L. Liu et al., 1997, 2007; Sobel and Arnaud, 1999; Wu et al., 2006, 2016; J.X. Zhang et al., 2005a, 2005b; Z.C. Zhang et al., 2010b).

Based on the age of the high-pressure and low-temperature (HP/LT) metamorphic rocks in the North Altun, Zhang et al. (2007) suggested that slab subduction began ca. 520 Ma. This is consistent with the presence of arc-related granitic rocks and the occurrence of early Paleozoic ophiolites in the belt (Gai et al., 2015; Gao et al., 2012; Yang et al., 2008). However, the tectonic evolution of this area was divided into different stages by previous scholars (e.g., Han et al., 2012; Liu et al., 2016; Meng et al., 2017). In addition, the early Paleozoic tectonic evolution, especially the subduction history of the belt, has not yet been characterized (Meng et al., 2017).

Mafic rocks are known to occur in the North Altun (Xinjiang BGMR, 1981, 2006), but little is known about their geochronology or petrogenesis or their relationship with the widespread silicic magmatism. Mafic rocks have different geochemical features that result from the different tectonic settings in which they formed. These features can also be used to constrain the nature of the mantle source (Hollanda et al., 2006; Yang and Zhou, 2009), the extent of metasomatism by subduction-related materials (Kepezhinskas et al., 1997), and the degree of interaction between mantle-derived magmas and crustal materials (DePaolo, 1981). Therefore, a detailed study on the mafic rocks in the North Altun can potentially provide significant information on the geodynamic evolution of the region.

Xian-Tao Ye http://orcid.org/0000-0002-6370-3323

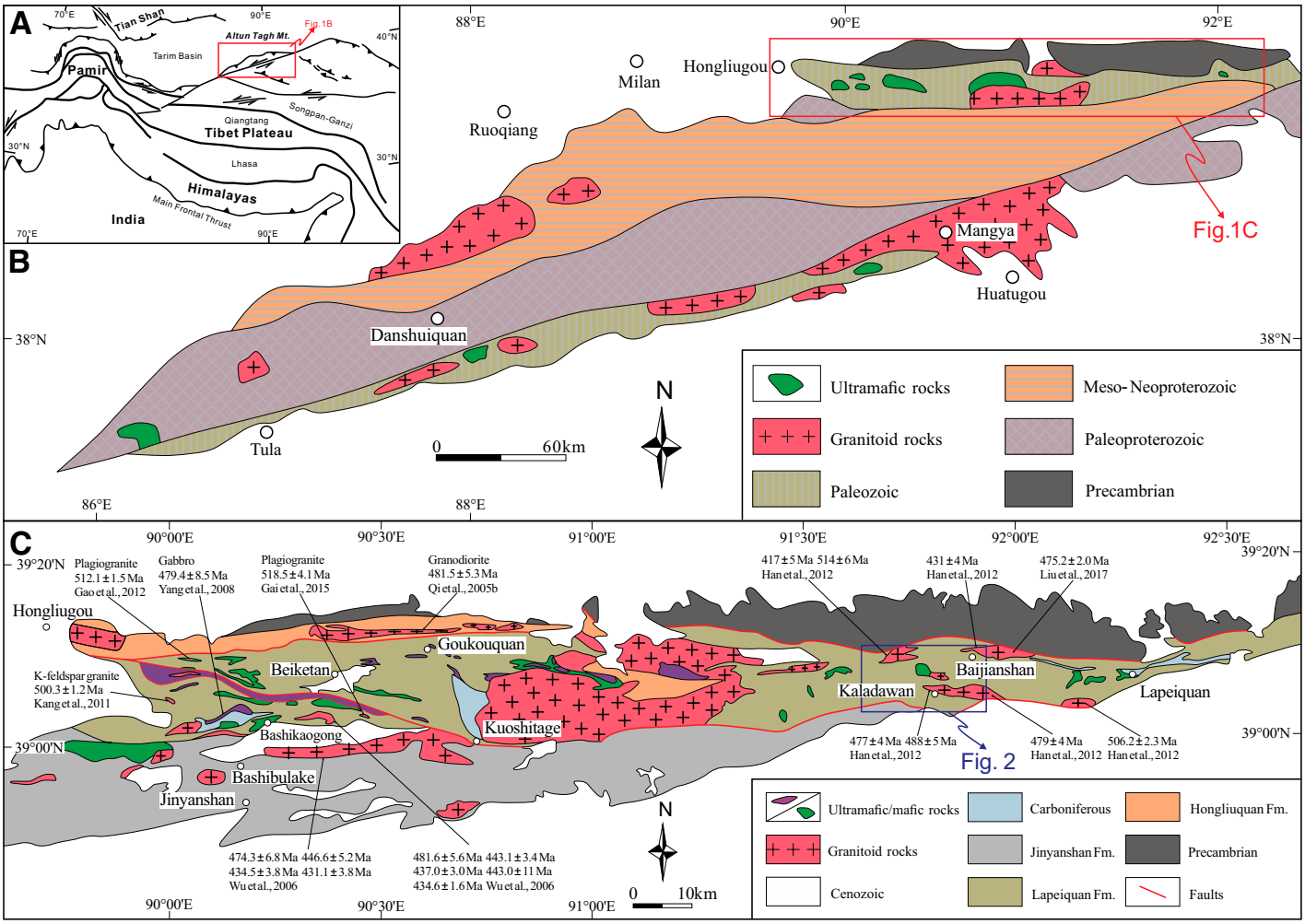


**Figure 1. (A) Simplified tectonic map of the Indo-Asian collision zone showing major active structures and suture zones (modified after Burtman and Molnar, 1993; Yin and Harrison, 2000). (B) Geologic and tectonic map of the Altun orogen (modified after Liu et al., 2002). (C) Geologic map of the North Altun (modified after Liu et al., 2007).**

In this study, we report detailed field observations, petrography, ages, and comprehensive geochemistry analyses of the mafic intrusions and andesitic lavas occurring in the volcanic-sedimentary sequence in the Kaladawan area at the northern margin of the Altun orogen. The main objectives of this study were to: (1) refine the previously invoked tectonic model based on the distinct metamorphism and multiphase emplacement of the ophiolites, and (2) elucidate the subduction/collision-induced extension in the Altun orogenic belt.

## REGIONAL GEOLOGY

The Altun orogen lies between the Tarim Basin to the north and the Qaidam Basin, Kunlun Mountains, and Tibetan Plateau to the south (Fig. 1A). From north to south, the Altun orogen can be divided into four tectonic units: the North Altun Archean complex (or the Dunhuang block), the North Altun oceanic subduction-collision complex, the Central Altun block (also known as the Milanhe-Jinyanshan block), and the South Altun continental-type subduction-collision complex (Fig. 1B; L. Liu et al., 2007, 2009, 2012; Wu et al., 2009; Zhang et al., 2014). The North Altun subduction complex consists of early Paleozoic volcanic-sedimentary sequences, ophiolites, high-pressure metamorphic rocks, and various granitic rocks. The volcanic-sedimentary sequence is termed the Lapeiquan Formation (or Kaladawan Formation; Xinjiang BGMR, 2006), outcropping extensively along the North Altun. Previous geological investigations considered the Lapeiquan Formation as a Mesoproterozoic (Xinjiang BGMR, 1981) or Ordovician sequence (Xinjiang BGMR, 2006). However, detrital zircons from the Lapeiquan Formation yielded a youngest peak age of ca. 920 Ma (Chen et al., 2009; Gehrels et al., 2003), indicating that its depositional age is younger than Mesoproterozoic. Ophiolites are distributed sporadically between the areas of Hongliugou and Lapeiquan, and they consist primarily of serpentinized peridotite (harzburgite), cumulates (wehrlite, gabbro, anorthosite, plagiogranite), and basalts. Zircon U-Pb ages of the cumulates range from 520 to 480 Ma (Gai et al., 2015; Gao et al., 2012; Yang et al., 2008; Zhang et al., 2015), and the ophiolites have been interpreted to have formed in a suprasubduction-zone setting (Dong et al., 2013; Guo et al., 1998; Yang et al., 2008). Blueschists and eclogites occur as lenses surrounding the metapelites in the area of the Hongliugou ophiolites (Che et al., 1995). Phengite from eclogites yielded a $^{40}Ar$-$^{39}Ar$ plateau age of 512 ± 3 Ma, and paragonite from blueschists gave a $^{40}Ar$-$^{39}Ar$ plateau age of 491 ± 3 Ma. These geochronological data indicate that the blueschists and

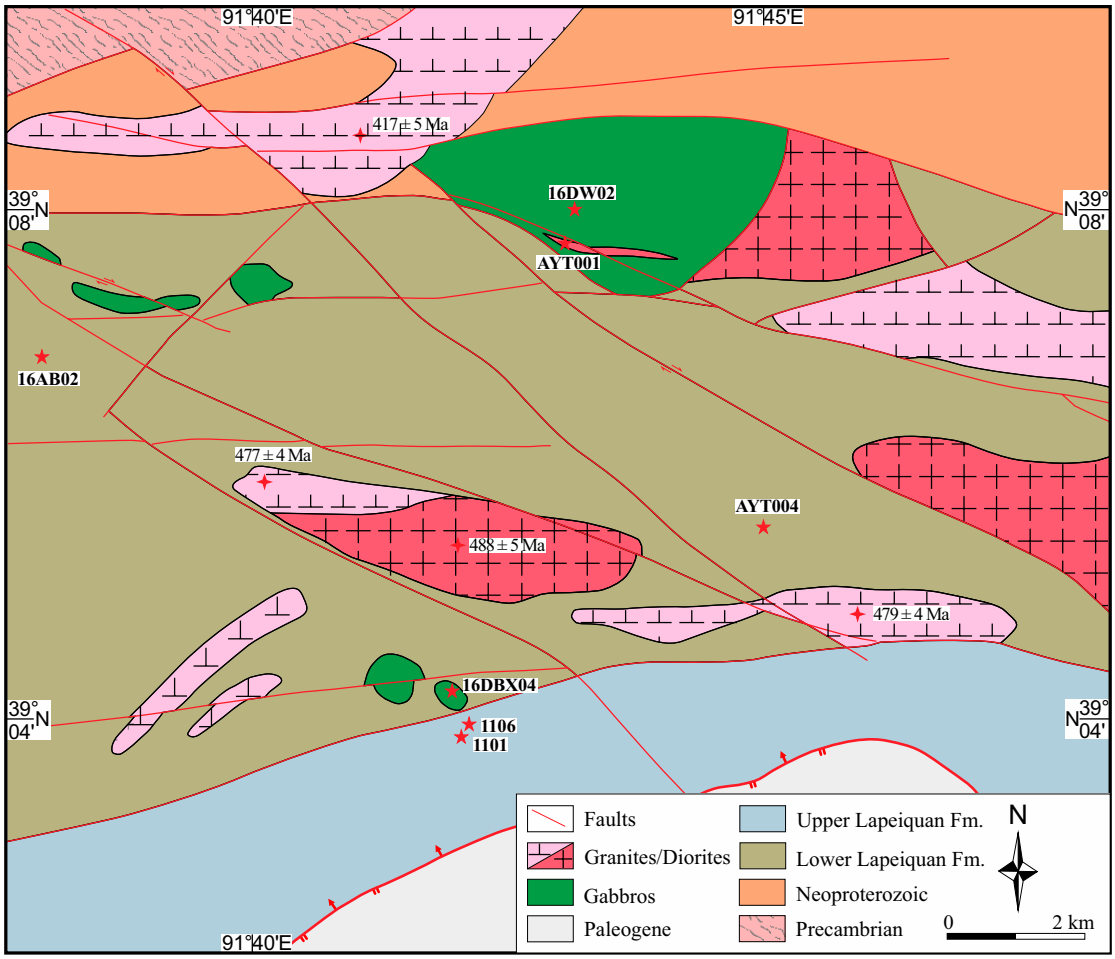


**Figure 2. Geologic map of the Kaladawan area, North Altun (modified after Xinjiang BGMR, 2006). Numbers and stars show the sample number and the sampling locality; the marked age data are from Han et al. (2012).**

eclogites formed during 510–490 Ma (Zhang and Meng, 2006; J.X. Zhang et al., 2005b, 2007, 2010). Granitoids can be subdivided into two groups: 520–470 Ma subduction-related I-type granites (Han et al., 2012; Kang et al., 2011; C. Liu et al., 2016; J.H. Liu et al., 2017; Wu et al., 2006) and 440–410 Ma I- and S-type anorogenic granites (Chen et al., 2003, 2009; Han et al., 2012; Z.C. Zhang et al., 2010b). Based on the presence of HP/LT metamorphic assemblages, and ophiolitic, subduction-accretion complex, and arc magmatic rocks, Zhang et al. (2015) proposed that the North Altun could be considered as a typical early Paleozoic accretionary orogenic belt.

Compared to the extensive distribution of granitoids along the North Altun, rare gabbroic intrusions occurred in this area. These intrusions form an E-W–trending belt from Hongliugou to Lapeiquan (Fig. 1C). The Kaladawan area, located in the eastern North Altun, hosts the Lapeiquan Formation, granitoids, and several mafic intrusions (Dawan and Dabanxi intrusions) and the Dawan mafic dikes. However, the emplacement ages, petrogenesis, and tectonic regime of these mafic rocks remain unknown.

## FIELD OBSERVATION AND SAMPLE COLLECTION

### Lapeiquan Formation

The Lapeiquan Formation is divided into lower and upper sections, outcropping along the Hongliugou-Lapeiquan ophiolite belt (Figs. 2 and 3A). The Lapeiquan Formation unconformably overlies the Neoproterozoic Muzisayi Formation. At its southern margin, it connects with the Paleogene Gancaigou Formation by a thrust fault. The lower section of the Lapeiquan Formation consists mainly of layers of mafic to silicic volcanic and volcaniclastic rocks, including basalt, andesite, dacite, rhyolite, and sericite-chlorite (quartz) schist (Fig. 3B; Ni et al., 2017; Xinjiang BGMR, 2006). In addition, it hosts a massive iron-ore deposit (Qi et al., 2008). The upper section of the Lapeiquan Formation is composed chiefly of clastic rocks, interbedded with minor metavolcanics and carbonates (Fig. 3C). It underwent lower-greenschist-facies metamorphism and tightly folded deformation. The upper Lapeiquan Formation sedimentary sequence extends more than 100 km from Qiongtage to the Lapeiquan area. Field and thin section observations have revealed that the major rock types are sericite-chlorite (quartz) schist, fine-grained sandstone, rhyolite, phyllite, ignimbrite, and dolomite. Lower-greenschist-facies metamorphic minerals such as biotite, sericite, and chlorite are commonly seen in most rock types. It should be noted that the upper Lapeiquan Formation hosts a large Pb-Zn-Ag-Cu polymetallic ore deposit in this region.

One rhyolite sample from the lower Lapeiquan Formation (16AB02: 39°07′14″N, 91°37′51″E; Fig. 4A) and two rhyolite samples from the upper Lapeiquan Formation (1101: 39°03′40″N, 91°37′51″E and 1106: 39°07′14″N, 91°37′51″E; Fig. 4B) were collected for zircon U-Pb dating. Ten andesitic samples (39°05′22″N, 91°44′55″E) were collected for

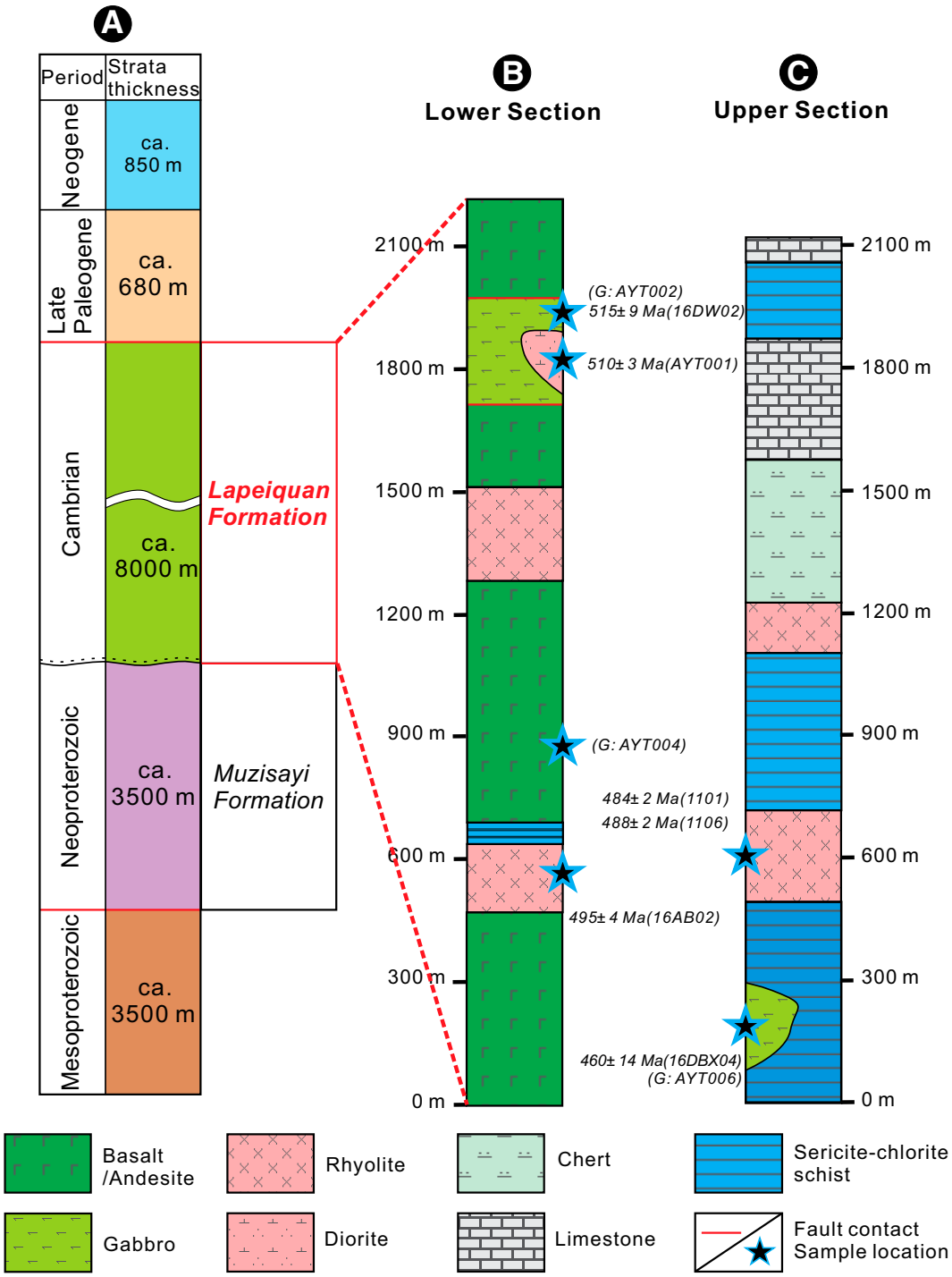


**Figure 3. (A) Simplified stratigraphic column from the Mesoproterozoic to the Neogene in the Kaladawan area (modified after Xinjiang BGMR, 2006). (B, C) Lower Lapeiquan Formation and upper Lapeiquan Formation stratigraphy in the Kaladawan area, showing the relationship of the volcanics and the intrusive rocks. G—geochemical samples.**

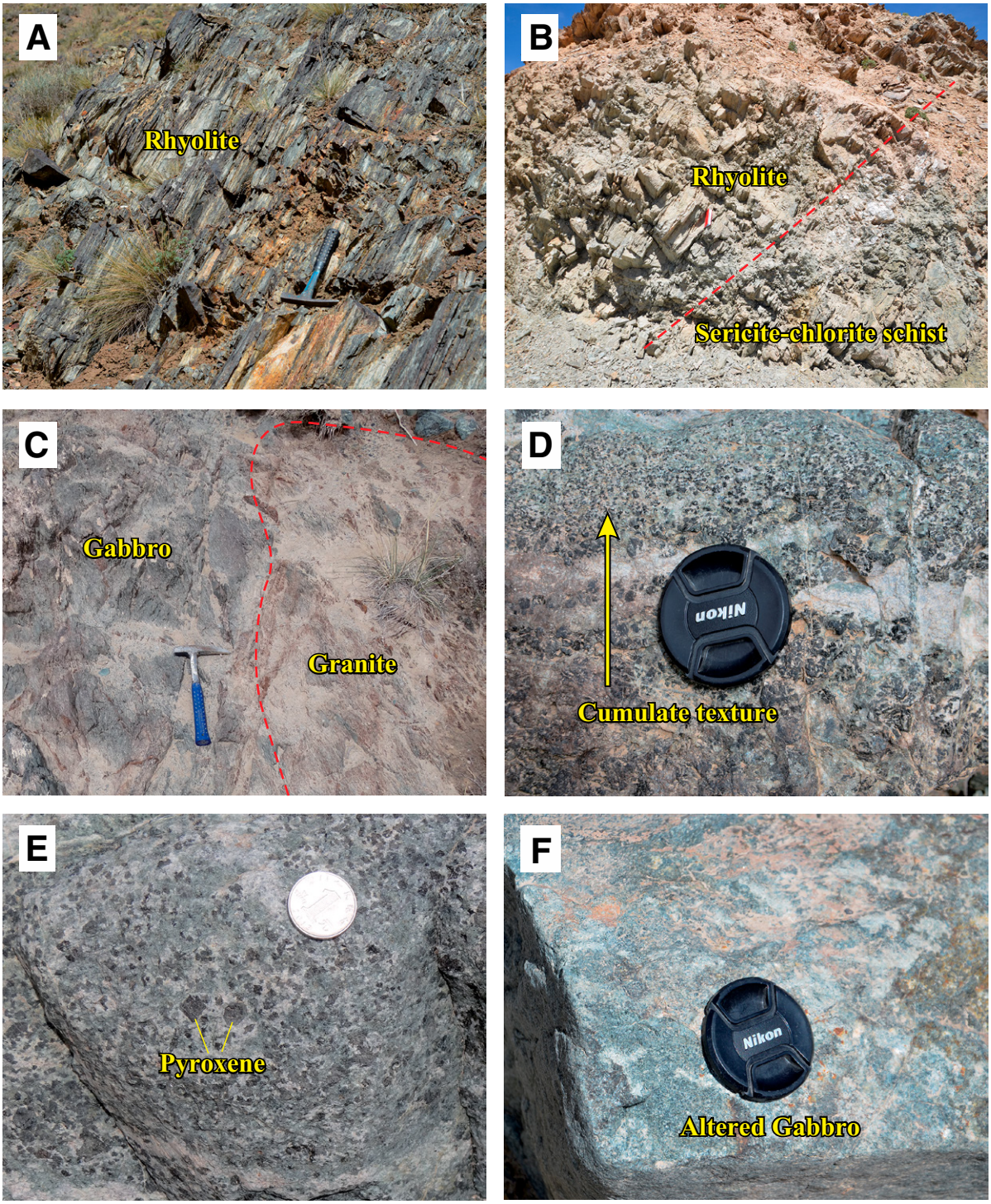


**Figure 4. Field photographs of the Dawan mafic intrusion, rhyolite from the lower and upper Lapeiquan Formation, and the Dabanxi mafic intrusion: (A) cumulate structure of the Dawan gabbros; (B) euhedral pyroxenes in the Dawan gabbros; (C) intrusive contact between the Dawan mafic intrusion and granitic rocks; (D) interbedded rhyolite layer from the lower Lapeiquan Formation; (E) relationship between the rhyolite and sericite-chlorite schist from the upper Lapeiquan Formation; and (F) alteration of gabbro from the Dabanxi mafic intrusion.**

geochemical work. Rhyolites have euhedral to subhedral crystal plagioclase and potassium feldspar (K-feldspar; Figs. 5A and 5B), whereas andesites contain plagioclase (30%–45%), hornblende (40%–45%), K-feldspar (5%–10%), quartz (5%–10%), and minor epidote, zircon, and apatite (Fig. 5C).

### Dawan Intrusion

The Dawan gabbroic intrusion is one of the largest mafic intrusions in the Kaladawan area. It shares a fault contact with country rocks (Xinjiang BGMR, 2006), and then is intruded by a granitic pluton (Fig. 4C). Massive structure and cumulate texture are evident. Rhythmic layering of plagioclase and pyroxene is commonly observed at several outcrops in the field (Fig. 4D). The gabbro has typical gabbroic texture with euhedral to semi-euhedral pyroxene and plagioclase in both outcrop and thin sections (Figs. 4E, 5D, and 5E). The main minerals are clinopyroxene (40%–50%) and plagioclase (30%–45%). The minor minerals include hornblende and epidote. Zircon, titanite, and apatite are present as accessory minerals. One geochronological sample (16DW02: 39°08′08″N, 91°43′19″E) and seven geochemical samples were collected from this pluton. In addition, one sample from the granitic pluton intruding the gabbro (AYT001: 39°08′31″N, 91°42′5″E) was collected for geochronological analysis.

### Dabanxi Intrusion

In the Kaladawan area, dozens of E-W–trending mafic intrusions and dikes were emplaced in the lower Lapeiquan Formation (Fig. 2). Among them, the Dabanxi intrusion, of coarse-grained texture and with a total outcrop area of ~1 km$^2$, is relatively suitable for zircon selection.

The dominant rocks of the Dabanxi stocks are coarse- to medium-grained gabbros (Fig. 4F). The gabbros are generally composed of euhedral crystals of plagioclase and clinopyroxene, with minor hornblende, biotite, apatite, and Fe-Ti oxides. Most of the gabbros have experienced

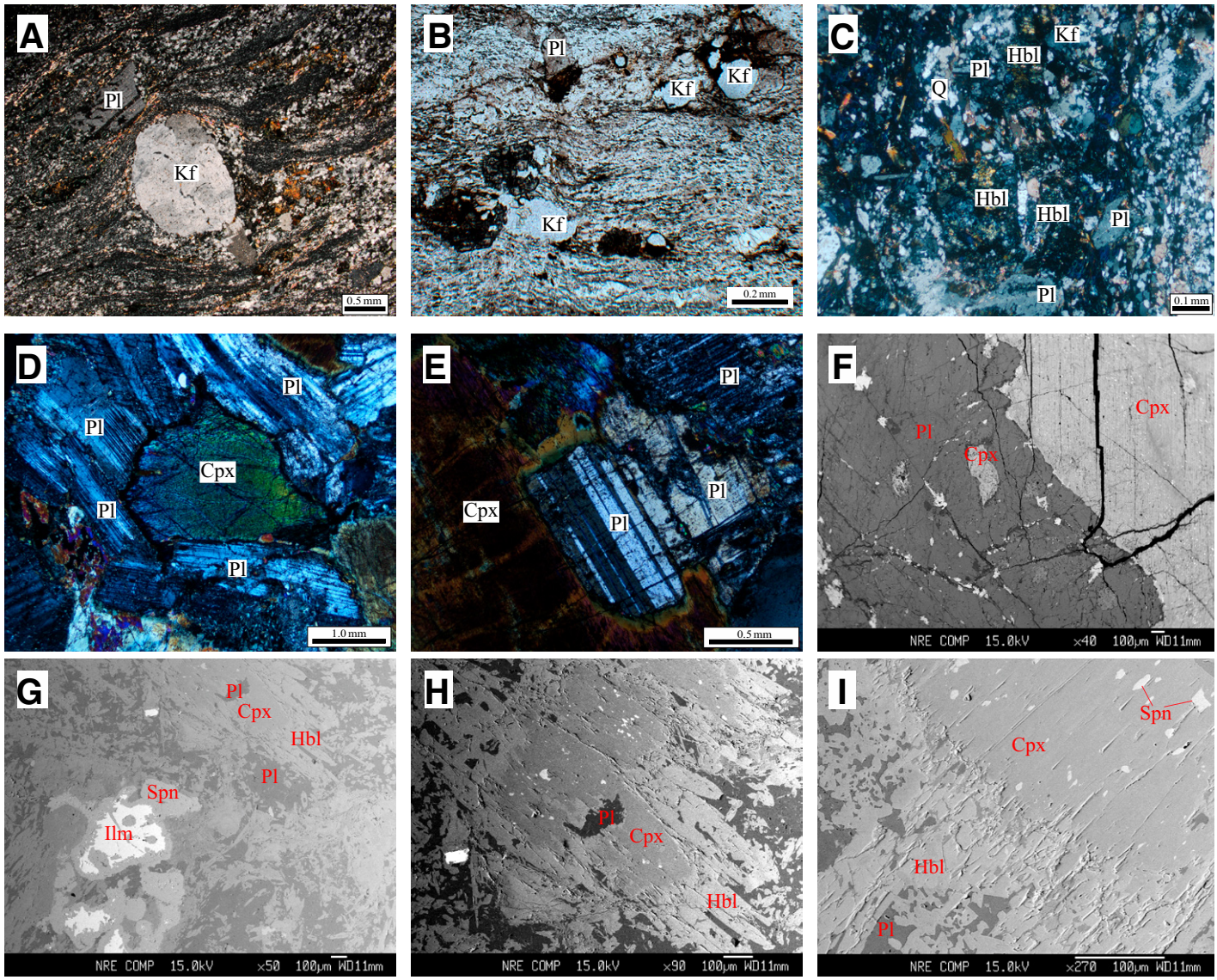


**Figure 5. Photomicrographs of: (A, B, C) Dawan gabbros, (D) rhyolite from the lower Lapeiquan Formation, (E) rhyolite from the upper Lapeiquan Formation, (F) andesite from the lower Lapeiquan Formation, and (G, H, I) Dabanxi gabbros (see details in the text). Cpx—clinopyroxene; Hbl—hornblende; Ilm—ilmenite; Kf—K-feldspar; Pl—plagioclase; Q—quartz; Spn—sphene.**

variable degrees of alteration, resulting in albitization of some plagioclases and some alteration of clinopyroxene to amphibole, chlorite, or epidote (Fig. 5G). In thin section, the gabbro contains 40%–50% plagioclase and 45%–50% clinopyroxene, with minor hornblende, epidote, sphene, and Fe-Ti oxides (Figs. 5H and 5I). One sample for geochronology (16DBX04: 39°04′19″N, 91°41′55″E) and 10 samples for geochemical analyses were collected from this intrusion.

## ANALYTICAL METHODS

Zircon separation was carried out using conventional heavy liquid and magnetic separation techniques. Zircon grains were then handpicked under a binocular microscope, and representative grains and zircon standards (TEMORA) were mounted in epoxy resin disks. These were then polished to approximately half their thickness. Zircons were photographed under transmitted and reflected light, and cathodoluminescence (CL) images were taken to reveal their internal structures.

Zircon U-Pb analyses were carried out using sensitive high-resolution ion microprobe II (SHRIMP II) and laser ablation–inductively coupled plasma–mass spectrometry (LA-ICP-MS) techniques at the Beijing SHRIMP Center, Chinese Academy of Geological Sciences, and Tianjin Institute of Geology and Mineral Resources, respectively. Ion microprobe procedures followed those described by Williams (1998), whereas LA-ICP-MS analytical procedures were described by Geng et al. (2011) and Hou et al. (2009). Data reduction was performed off-line using ICPMS-DataCal (Liu et al., 2010a, 2010b). SQUID 1.0 and Isoplot (Ludwig, 1999) software were used for data processing. Zircon U-Pb age data are listed in Table DR1 in the GSA Data Repository Item.[1]

Clinopyroxene compositions were determined by wavelength-dispersion X-ray emission spectrometry using a JEOL JXA-8100 electron-probe microanalyzer (EMPA) at the State Key Laboratory Breeding Base of Nuclear Resources and Environment, Nanchang, China. Operating conditions were 15 kV accelerating voltage and 20 nA beam current, with a 10 s counting time. Representative mineralogical data are listed in Tables DR2 and DR3 in the GSA Data Repository Item.

Major elements were measured by using a Rigaku ZSX100e X-ray fluorescence spectrometer (XRF) at the State Key Laboratory of Ore Deposit Geochemistry, Institute of Geochemistry, Chinese Academy of Sciences (CAS). Whole-rock samples were crushed and powdered to less than 200 mesh in an agate mill, and then samples were fused with lithium-tetraborate glass pellets. Analytical precision as determined by Chinese National Standards GSR-1 and GSR-3 was generally ~1%–5%. Trace elements were analyzed using a Perkin-Elmer ELAN-DRC-e ICP-MS at the State Key Laboratory of Ore Deposit Geochemistry, Institute of Geochemistry, CAS. Powdered samples (50 mg) were digested in high-pressure Teflon bombs using an HF + $HNO_3$ mixture for 48 h at ~195 °C (Qi et al., 2000). Analytical precision for most elements was better than 3%–5%. Analytical results are presented in Table 1.

Samples for Nd-Sr isotopic measurement were spiked and dissolved in Teflon bombs with HF + $HNO_3$ acid and then separated by conventional cation-exchange techniques. The isotopic measurements were performed on a Thermo Fisher Triton TI thermal ionization mass spectrometer (TIMS) at the State Key Laboratory of Ore Deposit Geochemistry, Institute of Geochemistry, CAS. The detailed procedure we used is as described by Li et al. (2004). Measured $^{87}Sr/^{86}Sr$ and $^{143}Nd/^{144}Nd$ ratios were corrected to $^{86}Sr/^{88}Sr = 0.1194$ and $^{146}Nd/^{144}Nd = 0.7219$, respectively. The reported $^{87}Sr/^{86}Sr$ average ratios for the NBS987 standard and BCR-2 standard were $^{87}Sr/^{86}Sr = 0.710219 \pm 5$ (2σ) and $0.704966 \pm 3$ (2σ), respectively, and the $^{143}Nd/^{144}Nd$ average ratios for the LRIG and BCR-2 standards were $^{143}Nd/^{144}Nd = 0.512196 \pm 3$ (2σ) and $0.512634 \pm 4$ (2σ), respectively. Analytical results and calculated parameters are listed in Table 2.

## ANALYTICAL RESULTS

### Zircon U-Pb Ages

#### *Dawan Intrusion (Gabbroic Sample 16DW02 and Granitic Sample AYT001)*

Zircons in sample 16DW02 are euhedral, with average crystals size up to 50–80 μm and length-to-width ratios from 1:1 to 2:1. All zircons are colorless and without obvious zoning (Fig. 6). Fifteen grains were analyzed in this sample. Among them, five spots yielded younger ages, ranging from 222 to 406 Ma, which may reflect the effects of alteration and/or metamorphic events after emplacement, due to the absence of clear oscillatory growth zoning and presence of white or dark areas in their CL images. The other 10 spots have U and Th contents of 338–2989 ppm and 178–1678 ppm, respectively, with Th/U ratios varying from 0.11 to 0.91 (Table DR1). Most zircons show variable discordance between $^{206}Pb/^{238}U$ and $^{207}Pb/^{235}U$ ages but yield a discordance line with an intercept age of 524 ± 22 Ma (mean square of weighted deviates [MSWD] = 0.27; Fig. 7A). On the other hand, their $^{206}Pb/^{238}U$ ages are consistent within error and yield a weighted mean age of 515 ± 9 Ma (Fig. 7A), which is comparable to the intercept age.

Zircons from sample AYT001 are broadly euhedral (Fig. 6), with length ranging from 80 to 100 μm, and length-to-width ratio of 2:1. Thirty-two grains were analyzed on 32 grains. The data show variable U (275–1665 ppm) and Th (76–999 ppm) contents, with Th/U ratios of 0.28–0.96 (Table DR1). Excepting spots 07, 09, and 20, the other analyses define a good discordia with upper intercept age of 510 ± 3 Ma (MSWD = 0.54), and a weighted mean $^{206}Pb/^{238}U$ age of 511 ± 2 Ma (MSWD = 0.53; Fig. 7B).

#### *Lapeiquan Formation (Rhyolites 16AB02, 1101, and 1106)*

Zircons in sample 16AB02 are transparent, euhedral prismatic grains with concentric zoning in CL images (Fig. 6), and they are ~80 μm in length with aspect ratios of 1:1 to 2:1. Fifteen grains were analyzed, which yielded variable U and Th contents (U = 254–525 ppm, Th = 109–345 ppm, Th/U = 0.42–0.69). All analyses were concordant within analytical errors and yielded a weighted mean $^{206}Pb/^{238}U$ age of 495 ± 4 Ma (MSWD = 0.45; Fig. 7C).

Zircons from samples 1101 and 1106 are transparent and pinkish in color, range from 100 to 150 μm in length, and have length-to-width ratios of 2:1 to 3:1. In CL images, interval growth zoning is clear in most of the zircon crystals, and no core-rim structure is observed (Fig. 6). In total, 32 analyses on sample 1101 showed that the concentrations of U and Th are in the ranges of 401–987 ppm and 161–445 ppm, respectively, with consistent Th/U ratios between 0.37 and 0.60 (Table DR1). The measured $^{206}Pb/^{238}U$ ages are in good agreement within analytical error and yield a weighted mean age of 484 ± 2 Ma (MSWD = 0.78; Fig. 7D). Sample 1106 has variable contents of U (250–2007 ppm) and Th (74–1103 ppm), with Th/U ratios of 0.30–0.85 (Table DR1). All 32 analyses form a tight cluster on a concordia plot and yield a weighted mean $^{206}Pb/^{238}U$ age of 488 ± 2 Ma (MSWD = 0.36; Fig. 7E).

[1]GSA Data Repository Item 2018355, Table DR1: SHRIMP (16DW02, 16AB02, and 16DBX04) and LA-ICP-MS (AYT001, 1101, and 1106) zircon U-Pb data; Table DR2: Composition of clinopyroxene in the gabbro from the Dawan intrusion; and Table DR3: Composition of clinopyroxene in the gabbro from the Dabanxi intrusion, is available at http://www.geosociety.org/datarepository/2018, or on request from editing@geosociety.org.

TABLE 1. GEOCHEMICAL COMPOSITIONS OF THE DAWAN INTRUSION, DAWAN HIGH-Mg ANDESITES, AND DABANXI INTRUSION

| Site | Dawan intrusion | | | | | | Dawan high-Mg andesites | | | | | | | | | | Dabanxi intrusion | | | | | | | | | |
|---|---|---|---|---|---|---|---|---|---|---|---|---|---|---|---|---|---|---|---|---|---|---|---|---|---|---|
| Rock | Gabbro | Gabbro | Gabbro | Gabbro | Gabbro | Gabbro | Andesite | Andesite | Andesite | Andesite | Andesite | Andesite | Andesite | Andesite | Andesite | Andesite | Gabbro | Gabbro | Gabbro | Gabbro | Gabbro | Gabbro | Gabbro | Gabbro | Gabbro | Gabbro |
| Sample | AYT002 H1 | AYT002 H2 | AYT002 H3 | AYT002 H5 | AYT002 H6 | AYT002 H7 | AYT004 H1 | AYT004 H2 | AYT004 H3 | AYT004 H4 | AYT004 H5 | AYT004 H6 | AYT004 H7 | AYT004 H8 | AYT004 H9 | AYT004 H10 | AYT006 H1 | AYT006 H2 | AYT006 H3 | AYT006 H4 | AYT006 H5 | AYT006 H6 | AYT006 H7 | AYT006 H8 | AYT006 H10 | AYT006 H10 |
| $SiO_2$ | 48.1 | 45.8 | 47.6 | 47.5 | 49.1 | 50.0 | 55.4 | 55.9 | 54.7 | 52.9 | 54.6 | 58.0 | 57.1 | 58.1 | 58.7 | 57.8 | 47.4 | 46.7 | 46.1 | 45.8 | 44.5 | 45.8 | 45.3 | 46.9 | 47.6 | 47.6 |
| $TiO_2$ | 0.25 | 0.69 | 0.25 | 0.21 | 0.47 | 0.20 | 0.610 | 0.65 | 0.57 | 0.58 | 0.65 | 0.92 | 1.14 | 0.95 | 0.98 | 0.91 | 1.01 | 0.88 | 0.94 | 1.00 | 1.00 | 0.90 | 0.97 | 0.92 | 1.52 | 1.56 |
| $Al_2O_3$ | 17.6 | 15.6 | 15.9 | 19.5 | 18.4 | 19.7 | 13.6 | 13.9 | 13.5 | 14.5 | 15.0 | 13.6 | 13.5 | 13.2 | 13.1 | 13.1 | 18.5 | 17.9 | 18.0 | 18.4 | 18.4 | 18.1 | 18.8 | 17.6 | 15.4 | 16.1 |
| $Fe_2O_3^T$ | 5.55 | 6.10 | 7.30 | 6.36 | 7.06 | 4.38 | 8.76 | 8.61 | 8.44 | 8.47 | 8.55 | 10.1 | 10.8 | 10.3 | 9.85 | 9.93 | 8.69 | 9.14 | 9.53 | 9.09 | 9.24 | 9.47 | 9.45 | 9.44 | 11.7 | 12.2 |
| MnO | 0.09 | 0.11 | 0.13 | 0.10 | 0.12 | 0.08 | 0.14 | 0.13 | 0.15 | 0.146 | 0.12 | 0.15 | 0.18 | 0.15 | 0.15 | 0.15 | 0.13 | 0.14 | 0.15 | 0.15 | 0.15 | 0.15 | 0.15 | 0.15 | 0.28 | 0.25 |
| MgO | 9.60 | 10.5 | 11.9 | 10.0 | 9.15 | 7.75 | 5.27 | 5.57 | 5.30 | 5.33 | 5.96 | 3.45 | 3.62 | 3.54 | 3.17 | 3.45 | 9.29 | 10.1 | 10.1 | 9.94 | 11.6 | 10.7 | 10.3 | 9.87 | 8.40 | 8.44 |
| CaO | 14.6 | 16.4 | 11.7 | 11.5 | 11.1 | 12.3 | 8.25 | 8.19 | 8.31 | 8.93 | 7.95 | 4.66 | 3.88 | 4.98 | 4.65 | 5.61 | 9.86 | 9.65 | 9.66 | 9.25 | 9.49 | 9.72 | 9.97 | 10.3 | 10.9 | 9.11 |
| $Na_2O$ | 1.73 | 1.35 | 1.19 | 1.47 | 2.19 | 1.56 | 1.05 | 0.92 | 1.87 | 2.02 | 1.35 | 3.46 | 1.98 | 2.96 | 3.54 | 3.10 | 2.13 | 1.78 | 1.70 | 2.08 | 1.79 | 1.88 | 1.94 | 1.78 | 2.08 | 2.38 |
| $K_2O$ | 0.36 | 0.39 | 0.99 | 0.11 | 0.26 | 0.41 | 0.38 | 0.41 | 0.23 | 0.17 | 0.32 | 0.20 | 1.52 | 0.26 | 0.26 | 0.30 | 0.37 | 0.50 | 0.71 | 0.81 | 0.31 | 0.36 | 0.46 | 0.267 | 0.49 | 0.31 |
| $P_2O_5$ | 0.04 | 0.07 | 0.07 | 0.04 | 0.07 | 0.02 | 0.09 | 0.11 | 0.07 | 0.10 | 0.12 | 0.13 | 0.16 | 0.12 | 0.14 | 0.12 | 0.12 | 0.10 | 0.12 | 0.11 | 0.14 | 0.10 | 0.11 | 0.10 | 0.11 | 0.15 |
| LOI | 2.03 | 2.36 | 2.51 | 2.98 | 2.12 | 3.24 | 6.11 | 5.79 | 6.66 | 6.35 | 5.53 | 5.13 | 5.68 | 5.28 | 5.11 | 5.69 | 2.30 | 2.80 | 2.84 | 3.22 | 2.99 | 2.52 | 2.46 | 2.41 | 1.27 | 1.88 |
| Total | 100.0 | 99.4 | 99.6 | 99.8 | 100 | 99.6 | 99.7 | 100 | 99.9 | 99.5 | 100 | 99.8 | 99.6 | 99.8 | 99.6 | 100 | 99.8 | 99.7 | 99.8 | 99.9 | 99.6 | 99.7 | 99.8 | 99.8 | 99.7 | 99.9 |
| Mg# | 77 | 77 | 76 | 76 | 72 | 78 | 54 | 56 | 55 | 55 | 58 | 40 | 40 | 41 | 39 | 41 | 68 | 69 | 68 | 68 | 71 | 69 | 68 | 67 | 59 | 58 |
| Sc | 37.5 | 44.7 | 34.7 | 26.9 | 33.3 | 29.7 | 42.1 | 40.0 | 42.3 | 39.2 | 38.2 | 39.9 | 41.7 | 40.6 | 38.3 | 40.1 | 23.5 | 23.3 | 23.8 | 23.6 | 20.5 | 24.6 | 24.0 | 27.4 | 35.4 | 32.3 |
| V | 132 | 209 | 127 | 104 | 175 | 111 | 201 | 247 | 196 | 185 | 252 | 119 | 89.1 | 120 | 101 | 117 | 180 | 173 | 173 | 175 | 167 | 173 | 174 | 175 | 260 | 259 |
| Cr | 869 | 1080 | 645 | 515 | 334 | 824 | 212 | 326 | 224 | 205 | 326 | 109 | 61.1 | 107 | 85.4 | 104 | 273 | 306 | 272 | 277 | 303 | 290 | 272 | 367 | 264 | 308 |
| Co | 37.4 | 32.4 | 43.2 | 43.4 | 39.3 | 30.5 | 18.9 | 23.6 | 21.1 | 20.1 | 24.3 | 17.7 | 19.0 | 18.1 | 15.7 | 18.2 | 38.6 | 45.9 | 44.1 | 44.9 | 48.9 | 44.7 | 42.4 | 44.7 | 43.1 | 45.4 |
| Ni | 145 | 125 | 132 | 153 | 139 | 140 | 4.00 | 3.88 | 4.50 | 6.12 | 5.40 | 3.12 | 2.42 | 3.56 | 3.06 | 3.82 | 139 | 179 | 168 | 171 | 206 | 176 | 156 | 142 | 95.4 | 103 |
| Ga | 11.7 | 11.1 | 10.8 | 12.1 | 13.4 | 12.5 | 16.8 | 15.7 | 15.4 | 15.2 | 16.5 | 17.2 | 18.4 | 17.7 | 17.0 | 16.9 | 14.3 | 14.8 | 14.6 | 14.6 | 14.0 | 14.2 | 14.0 | 14.1 | 14.7 | 17.3 |
| Rb | 14.3 | 16.7 | 39.2 | 2.73 | 9.27 | 15.3 | 20.3 | 20.6 | 9.54 | 6.00 | 14.3 | 7.83 | 62.8 | 10.2 | 9.36 | 11.7 | 16.3 | 22.3 | 30.0 | 49.1 | 14.5 | 15.8 | 20.7 | 11.3 | 14.7 | 8.22 |
| Sr | 179 | 140 | 187 | 205 | 201 | 201 | 152 | 186 | 181 | 179 | 161 | 103 | 104 | 95.2 | 94.7 | 89.5 | 261 | 280 | 285 | 252 | 237 | 248 | 258 | 258 | 261 | 255 |
| Y | 5.83 | 13.6 | 5.72 | 4.52 | 14.9 | 5.11 | 24.2 | 25.4 | 23.2 | 21.1 | 23.7 | 31.7 | 35.4 | 31.9 | 34.8 | 32.6 | 20.8 | 16.6 | 18.5 | 16.1 | 16.7 | 17.4 | 19.5 | 15.4 | 28.4 | 27.1 |
| Zr | 6.46 | 27.4 | 7.32 | 4.94 | 25.8 | 6.20 | 72.5 | 80.6 | 65.3 | 58.8 | 74.2 | 102 | 136 | 102 | 113 | 105 | 52.2 | 46.5 | 42.6 | 48.9 | 52.8 | 48.5 | 45.3 | 42.5 | 65.8 | 69.3 |
| Nb | 0.545 | 1.49 | 0.496 | 0.329 | 1.33 | 0.835 | 4.36 | 4.66 | 4.01 | 3.80 | 4.28 | 6.07 | 8.19 | 6.18 | 6.65 | 6.26 | 2.22 | 1.63 | 1.67 | 1.88 | 1.86 | 1.58 | 1.70 | 1.42 | 3.00 | 2.94 |
| Cs | 0.559 | 1.21 | 0.997 | 0.255 | 0.644 | 0.970 | 0.555 | 0.455 | 0.199 | 0.156 | 0.345 | 0.246 | 0.590 | 0.354 | 0.175 | 0.427 | 0.173 | 0.156 | 0.175 | 0.227 | 0.148 | 0.195 | 0.169 | 0.109 | 0.0723 | 0.0668 |
| Ba | 99.8 | 73.8 | 153 | 33.8 | 80.0 | 159 | 58.4 | 67.5 | 51.5 | 44.8 | 68.0 | 54.9 | 387 | 59.5 | 70.5 | 73.4 | 109 | 108 | 148 | 148 | 70.4 | 92.5 | 119 | 61.9 | 133 | 78.5 |
| La | 0.851 | 2.19 | 3.81 | 0.611 | 2.20 | 1.04 | 11.9 | 11.8 | 9.24 | 10.1 | 12.9 | 17.9 | 20.2 | 17.9 | 18.6 | 16.9 | 4.31 | 3.28 | 3.49 | 3.47 | 3.95 | 3.64 | 3.89 | 3.09 | 5.46 | 5.56 |
| Ce | 2.00 | 5.57 | 6.49 | 1.48 | 5.86 | 2.46 | 24.4 | 24.7 | 19.5 | 22.3 | 27.2 | 36.9 | 41.8 | 36.1 | 39.0 | 36.0 | 9.87 | 8.65 | 8.77 | 9.22 | 10.5 | 8.72 | 9.41 | 8.11 | 13.5 | 13.8 |
| Pr | 0.276 | 0.811 | 0.613 | 0.210 | 0.860 | 0.309 | 2.67 | 2.88 | 2.40 | 2.63 | 3.17 | 4.28 | 4.88 | 4.28 | 4.46 | 4.07 | 1.45 | 1.23 | 1.30 | 1.22 | 1.47 | 1.28 | 1.34 | 1.16 | 1.97 | 2.03 |
| Nd | 1.42 | 4.26 | 2.46 | 1.18 | 4.45 | 1.51 | 10.5 | 11.1 | 9.44 | 10.5 | 12.3 | 16.7 | 19.1 | 16.1 | 17.6 | 16.0 | 7.07 | 5.66 | 6.29 | 6.08 | 7.20 | 6.03 | 6.65 | 5.79 | 9.50 | 9.92 |
| Sm | 0.550 | 1.51 | 0.794 | 0.429 | 1.52 | 0.505 | 2.27 | 2.39 | 2.18 | 2.58 | 2.99 | 3.87 | 4.57 | 3.95 | 3.90 | 3.82 | 2.21 | 1.82 | 1.89 | 1.90 | 2.10 | 1.82 | 1.92 | 1.68 | 2.74 | 2.94 |
| Eu | 0.354 | 0.556 | 0.421 | 0.333 | 0.612 | 0.311 | 0.668 | 0.689 | 0.624 | 0.823 | 0.817 | 0.880 | 0.889 | 0.850 | 0.805 | 0.820 | 0.923 | 0.803 | 0.874 | 0.879 | 0.942 | 0.849 | 0.888 | 0.820 | 1.17 | 1.27 |
| Gd | 0.792 | 1.94 | 0.923 | 0.647 | 2.01 | 0.600 | 2.77 | 2.93 | 2.58 | 3.05 | 3.53 | 4.58 | 5.04 | 4.37 | 4.76 | 4.32 | 2.91 | 2.20 | 2.46 | 2.40 | 2.65 | 2.37 | 2.75 | 2.20 | 3.67 | 3.83 |
| Tb | 0.139 | 0.345 | 0.169 | 0.122 | 0.366 | 0.124 | 0.488 | 0.512 | 0.459 | 0.543 | 0.613 | 0.810 | 0.888 | 0.790 | 0.839 | 0.764 | 0.539 | 0.404 | 0.450 | 0.437 | 0.471 | 0.421 | 0.498 | 0.378 | 0.674 | 0.667 |
| Dy | 1.04 | 2.50 | 1.17 | 0.884 | 2.58 | 0.838 | 3.37 | 3.58 | 3.19 | 3.61 | 4.06 | 5.40 | 6.16 | 5.29 | 5.80 | 5.30 | 3.60 | 2.64 | 3.11 | 2.80 | 3.05 | 2.92 | 3.26 | 2.63 | 4.43 | 4.44 |
| Ho | 0.227 | 0.570 | 0.263 | 0.177 | 0.571 | 0.172 | 0.735 | 0.795 | 0.688 | 0.824 | 0.927 | 1.23 | 1.36 | 1.19 | 1.28 | 1.20 | 0.778 | 0.610 | 0.646 | 0.602 | 0.687 | 0.632 | 0.677 | 0.554 | 0.942 | 0.976 |
| Er | 0.553 | 1.46 | 0.677 | 0.437 | 1.45 | 0.484 | 2.12 | 2.27 | 1.95 | 2.32 | 2.63 | 3.44 | 3.86 | 3.38 | 3.65 | 3.38 | 2.04 | 1.47 | 1.64 | 1.59 | 1.73 | 1.66 | 1.75 | 1.53 | 2.56 | 2.51 |
| Tm | 0.0794 | 0.200 | 0.0866 | 0.0620 | 0.223 | 0.0696 | 0.323 | 0.344 | 0.305 | 0.346 | 0.403 | 0.515 | 0.598 | 0.491 | 0.563 | 0.504 | 0.272 | 0.216 | 0.250 | 0.245 | 0.250 | 0.227 | 0.255 | 0.209 | 0.384 | 0.374 |
| Yb | 0.544 | 1.40 | 0.619 | 0.418 | 1.39 | 0.455 | 2.09 | 2.17 | 1.88 | 2.24 | 2.71 | 3.46 | 4.09 | 3.33 | 3.73 | 3.26 | 1.67 | 1.32 | 1.50 | 1.51 | 1.56 | 1.38 | 1.56 | 1.36 | 2.26 | 2.26 |
| Lu | 0.0844 | 0.202 | 0.0911 | 0.0593 | 0.207 | 0.0700 | 0.324 | 0.353 | 0.300 | 0.363 | 0.410 | 0.529 | 0.628 | 0.517 | 0.583 | 0.524 | 0.243 | 0.212 | 0.211 | 0.230 | 0.247 | 0.216 | 0.237 | 0.208 | 0.349 | 0.366 |
| Hf | 0.272 | 0.954 | 0.308 | 0.182 | 0.805 | 0.233 | 1.68 | 1.77 | 1.54 | 1.71 | 2.01 | 2.86 | 3.71 | 2.69 | 3.20 | 2.87 | 1.21 | 1.13 | 1.06 | 1.23 | 1.28 | 1.16 | 1.15 | 1.04 | 1.60 | 1.86 |
| Ta | 0.231 | 0.227 | 0.225 | 0.172 | 0.255 | 0.505 | 0.368 | 0.303 | 0.268 | 0.448 | 0.708 | 0.550 | 0.606 | 0.487 | 0.666 | 0.487 | 0.654 | 0.158 | 0.163 | 0.231 | 0.254 | 0.160 | 0.328 | 0.242 | 0.236 | 0.242 |
| Th | 0.212 | 0.246 | 0.126 | 0.0433 | 0.150 | 0.456 | 3.37 | 3.77 | 2.99 | 3.51 | 4.20 | 5.70 | 7.46 | 5.57 | 6.69 | 5.68 | 0.413 | 0.374 | 0.348 | 0.377 | 0.416 | 0.357 | 0.404 | 0.300 | 0.546 | 0.530 |
| U | 0.142 | 0.292 | 0.504 | 0.134 | 0.261 | 0.167 | 1.19 | 1.35 | 1.08 | 1.28 | 1.51 | 2.07 | 2.45 | 1.95 | 2.16 | 2.00 | 0.295 | 0.231 | 0.167 | 0.221 | 0.286 | 0.228 | 0.217 | 0.180 | 0.286 | 0.322 |

*Note*: Major oxides are given in wt%, and trace elements are given in ppm. LOI—loss on ignition.

TABLE 2. Sr-Nd ISOTOPIC COMPOSITIONS OF THE MAFIC ROCKS AND ANDESITES

| Sample | Rock type | Rb (ppm) | Sr (ppm) | $^{87}Rb/^{86}Sr$ | $^{87}Sr/^{86}Sr$ (2σ) | $(^{87}Sr/^{86}Sr)_i$ | Sm (ppm) | Nd (ppm) | $^{147}Sm/^{144}Nd$ | $^{143}Nd/^{144}Nd$ (2σ) | $(^{143}Nd/^{144}Nd)_i$ | $\varepsilon_{Nd}(t)$ |
|---|---|---|---|---|---|---|---|---|---|---|---|---|
| Dawan intrusion | | | | | | | | | | | | |
| AYT002H1 | Gabbro | 14.31 | 179 | 0.2313 | 0.706078 (22) | 0.70438 | 0.55 | 1.42 | 0.2342 | 0.513141 (18) | 0.5123508 | 7.4 |
| AYT002H2 | Gabbro | 16.74 | 140 | 0.3460 | 0.707840 (11) | 0.70530 | 1.51 | 4.26 | 0.2143 | 0.512989 (16) | 0.5122664 | 5.7 |
| AYT002H5 | Gabbro | 2.73 | 205 | 0.0385 | 0.705630 (12) | 0.70535 | 0.43 | 1.18 | 0.2198 | 0.513078 (14) | 0.5123366 | 7.1 |
| AYT002H6 | Gabbro | 9.27 | 201 | 0.1334 | 0.705600 (9) | 0.70462 | 1.52 | 4.45 | 0.2065 | 0.512700 (18) | 0.5120032 | 0.6 |
| Dawan high-Mg andesites | | | | | | | | | | | | |
| AYT004H2 | Andesite | 109.80 | 249 | 1.2775 | 0.720697 (7) | 0.71169 | 2.39 | 11.1 | 0.1302 | 0.512235 (19) | 0.5118131 | –3.7 |
| AYT004H6 | Andesite | 59.31 | 257 | 0.6685 | 0.719358 (11) | 0.71464 | 3.87 | 16.7 | 0.1401 | 0.512156 (21) | 0.5117014 | –5.8 |
| Dabanxi intrusion | | | | | | | | | | | | |
| AYT006H1 | Gabbro | 16.29 | 261 | 0.1806 | 0.707051 (7) | 0.70587 | 2.21 | 7.07 | 0.1890 | 0.512825 (27) | 0.5122551 | 4.1 |
| AYT006H6 | Gabbro | 15.84 | 248 | 0.1848 | 0.707204 (7) | 0.70599 | 1.82 | 6.03 | 0.1825 | 0.512626 (24) | 0.5120757 | 0.6 |
| AYT006H10 | Gabbro | 8.22 | 255 | 0.0932 | 0.708039 (6) | 0.70743 | 2.94 | 9.92 | 0.1792 | 0.512732 (26) | 0.5121918 | 2.9 |

*Note*: Chondritic uniform reservoir (CHUR) values ($^{87}Rb/^{86}Sr$ = 0.0847, $^{87}Sr/^{86}Sr$ = 0.7045; $^{147}Sm/^{144}Nd$ = 0.1967, $^{143}Nd/^{144}Nd$ = 0.512638) were used for the calculation. $\lambda_{Sm} = 6.54 \times 10^{-12}$ yr$^{-1}$ (Lugmair and Harti, 1978). The $(^{87}Sr/^{86}Sr)_i$, $(^{143}Nd/^{144}Nd)_i$, and $\varepsilon_{Nd}(t)$ values of samples AYT002, AYT006, and AYT004 were calculated using ages of 515 Ma, 460 Ma, and 495 Ma, respectively. The two-stage model age ($T_{2DM}$) calculations may be found in Jahn et al. (1999).

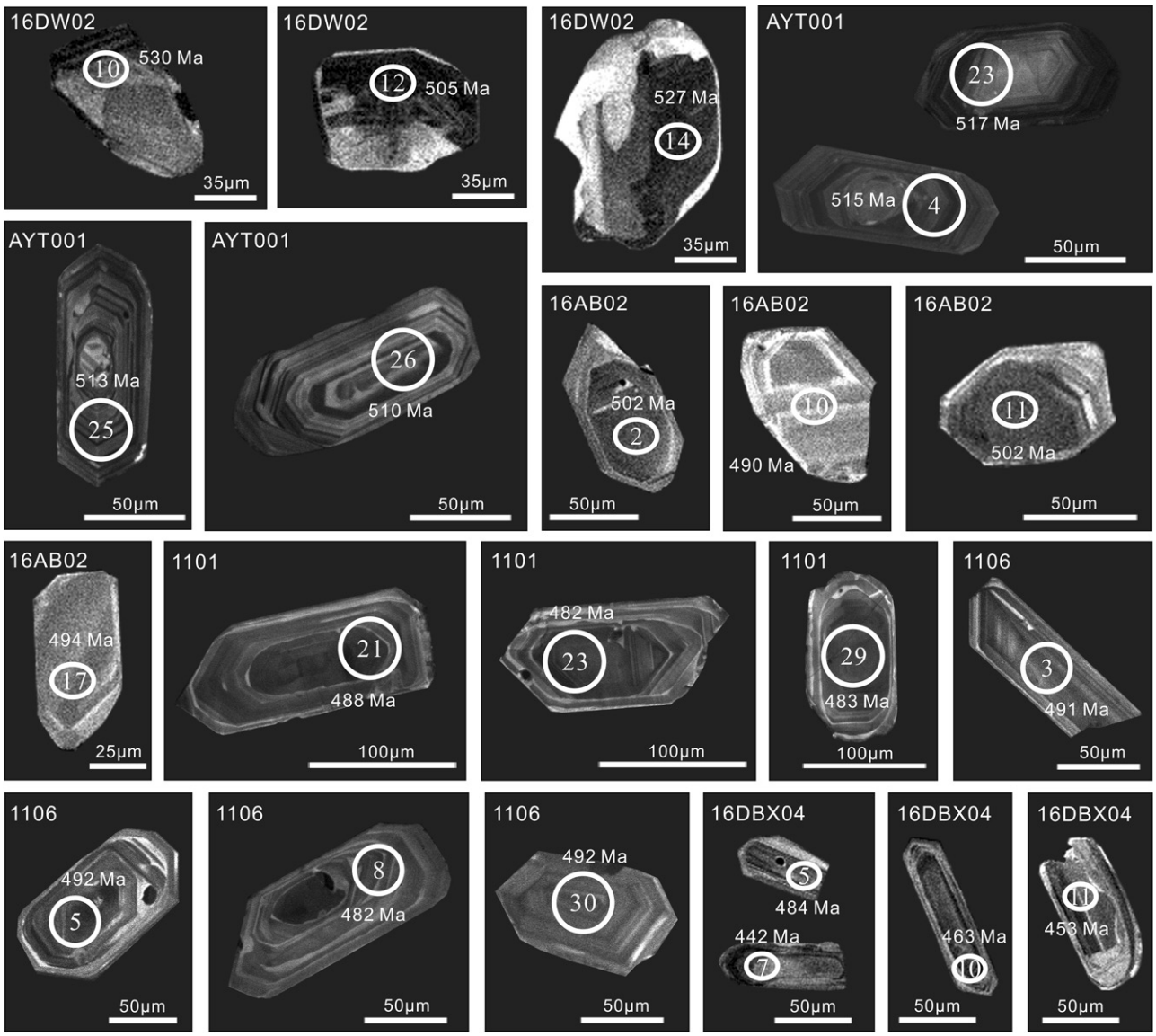


**Figure 6. Representative cathodoluminescence (CL) images of zircon from the Dawan mafic intrusion, rhyolites from the lower and upper Lapeiquan Formation, and the Dabanxi mafic intrusion. Analytical spots and ages are shown (see details in the text).**

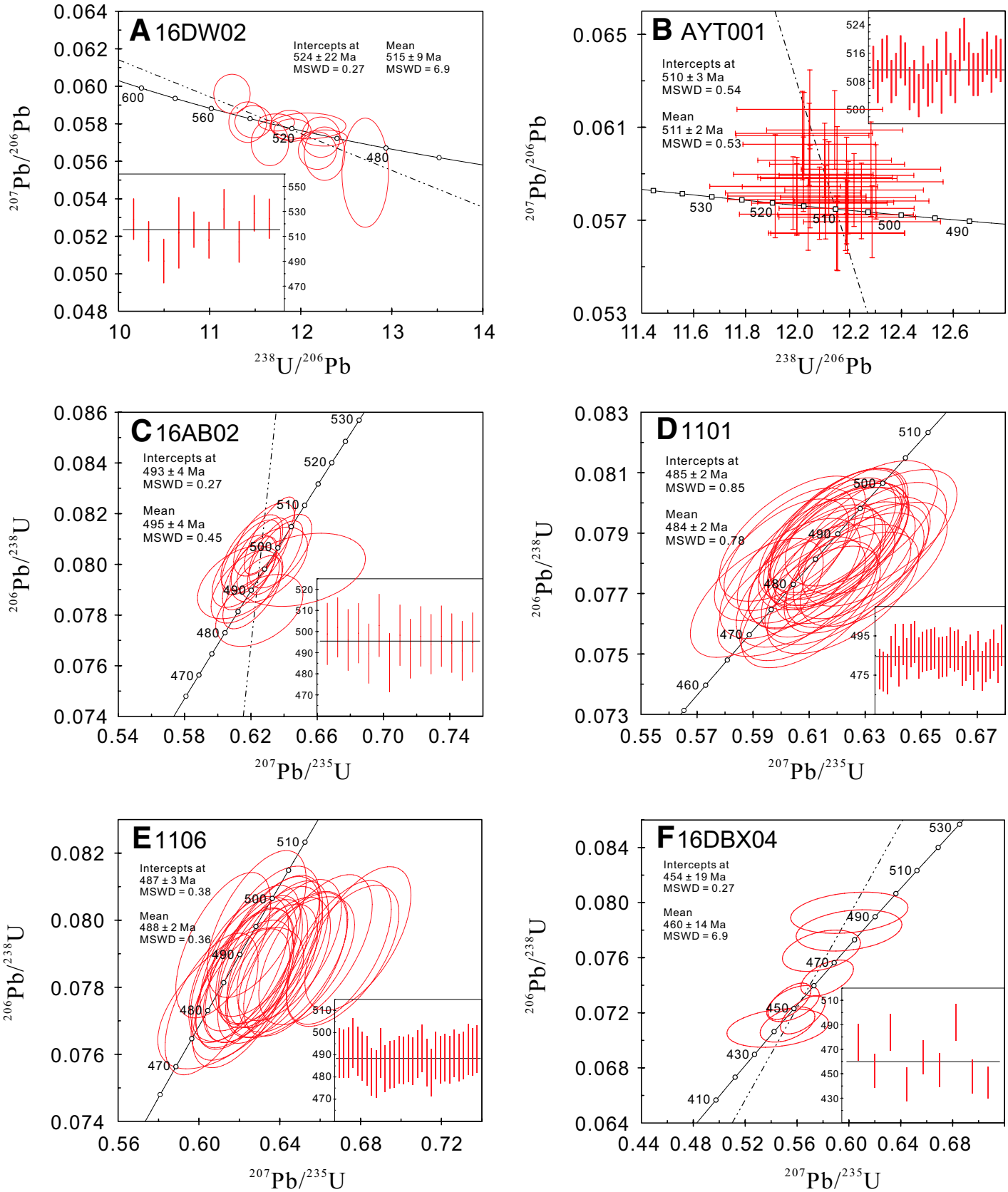


**Figure 7. Concordia plots of U-Pb zircon data for zircons from the Dawan mafic intrusion, rhyolites from the lower and upper Lapeiquan Formation, and the Dabanxi mafic intrusion. MSWD—mean square of weighted deviates.**

### *Dabanxi Intrusion (Gabbroic Sample 16DBX04)*

Zircons from sample 16DBX04 are transparent and are 50–150 μm in length, with length-to-width ratios between 1:1 and 3:1. Most zircons are prismatic crystals without obvious zoning in CL images (Fig. 6). Fifteen analyses were conducted on 15 zircons (Table DR1). Among them, nine analyses showed variable levels of U and Th, from 277 ppm to 947 ppm and from 96 ppm to 614 ppm, respectively, with Th/U ratios between 0.26 and 0.98. These nine analyses have concordant U-Pb ages and show a tight group, yielding a weighted mean $^{206}Pb/^{238}U$ age of 460 ± 14 Ma (MSWD = 6.9), which is interpreted as the crystallization age of the Dabanxi intrusion (Fig. 7F). Two analyses (spot-4 and spot-6) give slightly older $^{206}Pb/^{238}U$ ages from 545 Ma to 514 Ma (Table DR1). Results from another four spots (spot-2, spot-8, spot-9, and spot-12) give younger $^{206}Pb/^{238}U$ ages from 423 Ma to 296 Ma, with higher common Pb than the others, suggesting that the U-Pb isotopic system might have been modified during postemplacement alteration.

## Mineral Chemical Compositions

Nineteen clinopyroxene grains from the Dawan gabbros have $SiO_2$ contents between 48.90 and 52.70 wt%, CaO between 22.04 and 25.02 wt%, $TiO_2$ between 0.15 and 1.07 wt%, FeO between 4.98 and 6.17 wt%, and $Na_2O$ in the range of 0.26–0.84 wt%. Calculations using Minpet (version 2.02) indicated that the clinopyroxenes exhibit high Mg# (82–85). These clinopyroxenes are characterized by high Ca and low Ti, Al, and Na, and they plot in the diopside field in the Wo-En-Fs diagram (Fig. 8A), resembling clinopyroxenes from Alaskan-type complexes (Snoke et al., 1981; Helmy and El Mahallawi, 2003; Ye et al., 2015). Furthermore, they define a clear arc cumulate trend in the $Al^{VI}$ versus $TiO_2$ diagram (Figs. 8B and 8C; after Loucks, 1990).

Thirty-seven clinopyroxene grains from the Dabanxi gabbros were analyzed for chemical compositions (Table DR3). They have relative high $SiO_2$ (50.56–54.29 wt%) and $Al_2O_3$ (2.85–6.87 wt%) contents, low MgO (14.58–18.03 wt%), CaO (12.84–14.24 wt%), and $TiO_2$ (0–0.25 wt%) contents, and Mg# ranging from 66 to 78. They plot in the field of augite in the Wo-En-Fs diagram (Fig. 8A) and show arc-related features according to their $SiO_2$, $Al_2O_3$, and $TiO_2$ contents (Figs. 8B and 8C).

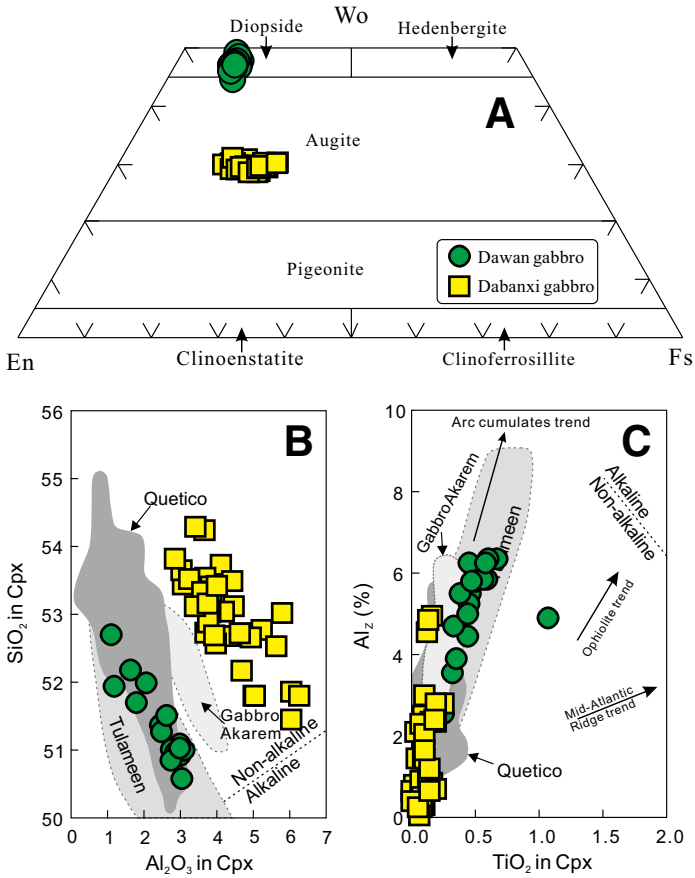


**Figure 8. (A) Wo-En-Fs diagram showing the compositions of the clinopyroxene from the Dawan intrusion; (B) $Al_2O_3$ (wt%) vs. $SiO_2$ (wt%) and (C) $TiO_2$ (wt%) vs. $Al^{IV}$ (percentage of tetrahedral site occupied by $Al_2$) in clinopyroxene from the Dawan intrusion. Gray fields are modified from Ye et al. (2015); reference lines of arc-related and rift-related tectonic environments are from Loucks (1990).**

## Whole-Rock Elemental Geochemistry

Seven gabbro samples from the Dawan intrusion, 10 andesite samples from the lower Lapeiquan Formation, and 10 gabbro samples from the Dabanxi intrusion were collected for major- and trace-element analyses (Table 1). The concentrations of major oxides, described below in weight percent, were recalculated to 100% on a volatile-free base.

All studied samples have undergone varying degrees of alteration, consistent with the observed fluctuation in loss on ignition (LOI) values (1.27–6.66 wt%). Thus, evaluation is required to assess the effects of alteration on the chemical compositions of these samples. Zirconium is conventionally regarded as an immobile element during low- to medium-grade alteration in igneous rocks (e.g., Wood et al., 1979). Therefore, a number of elements with different geochemical behaviors (e.g., Rb, Sr, Ba, Nb, La, Y, Th, U, and Ti) were plotted against Zr to evaluate their mobility during alteration (e.g., Fan et al., 2013). High field strength elements (HFSEs; Nb, Th, and Y), rare earth elements (REEs), U, and siderophile elements (such as Ti) showed strong correlations with Zr. In contrast, some large ion lithophile elements (LILEs; Rb, Sr, and Ba) were scattered over the plots (figure not shown). Consequently, mobile elements such as Rb, Sr, and Ba, and Sr isotopic compositions cannot be used in the geochemical classification and petrogenetic discussion.

### *Dawan Intrusion*

Gabbros from the Dawan intrusion have $SiO_2$ contents ranging from 47.2 to 51.9 wt% and display variable levels of $Fe_2O_3^T$ (4.54–7.52 wt%), $Al_2O_3$ (16.1–20.5 wt%), CaO (11.3–16.9 wt%), $TiO_2$ (0.21–0.71 wt%), $Na_2O$ (1.22–2.24 wt%), and $K_2O$ (0.11–1.02 wt%), owing to crystal fractionation/cumulation effects (Table 1). The gabbro samples plot in the subalkaline field of the total alkali-silica (TAS) diagram (figure not shown) and define a typical tholeiitic trend in the $TiO_2$ versus $FeO^{total}$/MgO diagram (Fig. 9B).

The Dawan gabbros contain variable compatible element contents, e.g., Cr ranges from 334 to 1080 ppm, Ni ranges from 125 to 153 ppm, and V ranges from 104 to 209 ppm, due to crystal fractionation/cumulation. On the other hand, they have low total REE contents between 7.0 and 24.3 ppm (Table 1). The gabbros mostly show flat chondrite-normalized REE patterns, with $(La/Yb)_N$ ranging from 0.99 to 1.07 (Fig. 10A). Significant positive Eu anomalies (δEu = 1.5–1.9) are observed in several samples (AYT002H1, AYT002H3, AYT002H5, AYT002H7), yet another two (AYT002H2 and AYT002H6) show no obvious Eu anomalies (δEu = 0.99–1.07; Fig. 10A). Normalized to primitive mantle, all samples exhibit variable enrichments in LILEs and pronounced Nb depletion (Nb/La = 0.13–0.80; Fig. 10B). The positive Sr anomalies are concurrent with the positive Eu anomalies, indicating plagioclase accumulation.

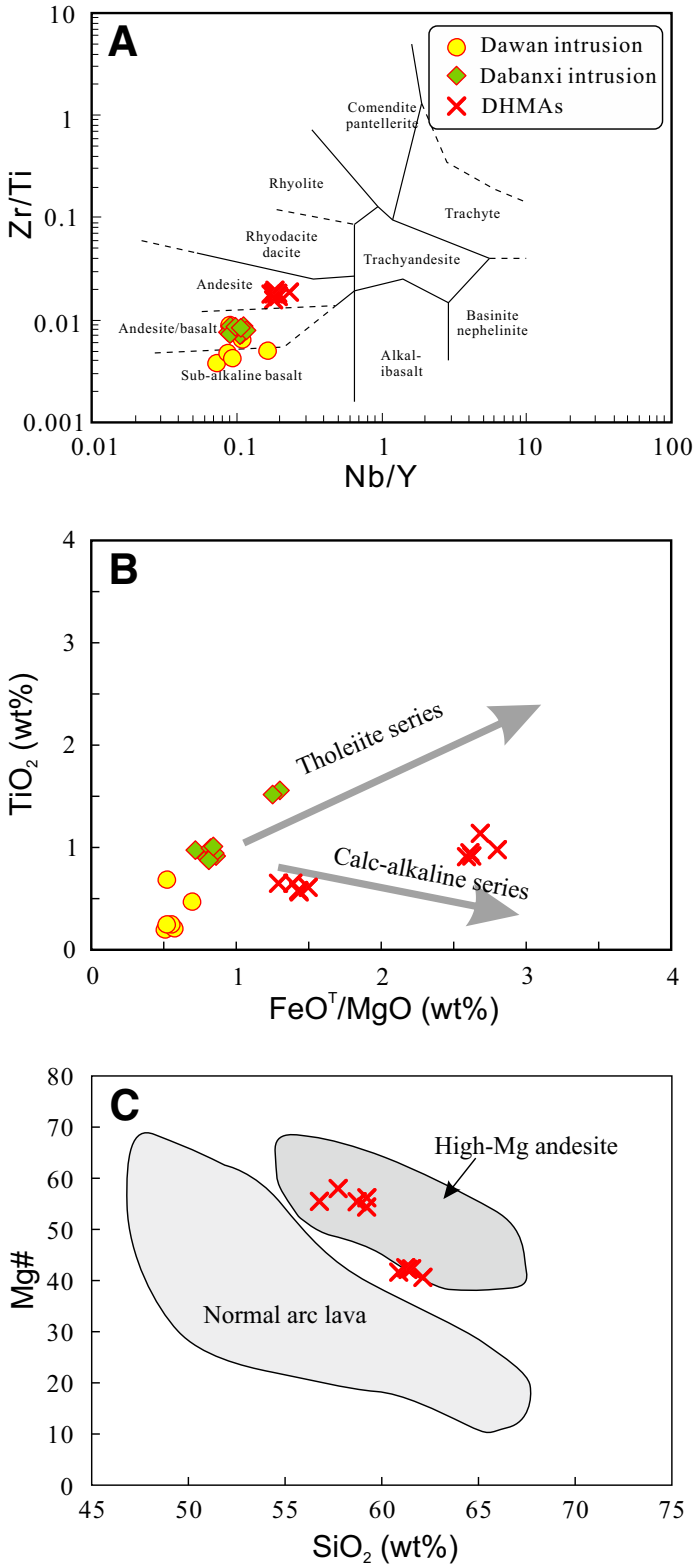


**Figure 9. (A) Incompatible elements (Zr/Ti vs. Nb/Y) classification diagram for the gabbros and andesites (Winchester and Floyd, 1977); (B) whole-rock $TiO_2$ (wt%) vs. $FeO^T$/MgO (wt%) plots for discrimination between the calc-alkaline and tholeiitic series, with calc-alkaline and tholeiitic fields after Miyashiro (1974); (C) Mg# vs. $SiO_2$ (wt%) classification diagrams for the andesites from the lower Lapeiquan Formation (Kelemen, 1995). DHMAs—Dawan high-Mg andesites.**

### *Dawan High-Mg Andesite*

Andesite samples display varied levels of $SiO_2$ (56.8–62.1 wt%), $Al_2O_3$ (13.9–15.8 wt%), $Fe_2O_3$ (9.04–11.5 wt%), MgO (3.35–6.30 wt%), $TiO_2$ (0.61–1.21 wt%), and total alkali ($Na_2O + K_2O$ = 1.52–4.02 wt%). These rocks plot in the field of andesite on the Zr–Ti-Nb–Y diagram (Fig. 9A; Winchester and Floyd, 1977), and they exhibit calc-alkaline trends in the $TiO_2$-$FeO^{total}$/MgO diagram (Fig. 9B). Furthermore, they can be classified as high-Mg andesite based on the Mg#-$SiO_2$ diagram (Fig. 9C).

Despite the observed variation in their REE abundances, all andesite samples display coherent REE patterns (ΣREE = 54.7–114 ppm). Chondrite-normalized REE patterns are markedly LREE-enriched (Fig. 10C), with $(La/Yb)_N$ values ranging from 3.04 to 3.84. They also display significant negative Eu anomalies (δEu = 0.57–0.90) and relatively flat heavy (H) REE patterns (normalized $[Gd/Yb]_N$ = 1.0–1.1; Table 1; Fig. 10C). Normalized to primitive mantle, all samples show variable degrees of depletion in HFSEs, such as Nb (Fig. 10D), thereby sharing an arc-related signature.

### *Dabanxi Intrusion*

Gabbros from the Dabanxi intrusion have $SiO_2$ contents varying from 46.1 to 48.7 wt%, with relatively high MgO (8.53–12.0 wt%), $Al_2O_3$ (15.7–19.1 wt%), and $TiO_2$ (0.90–1.59 wt%) contents, but relatively low levels of total alkalis ($Na_2O + K_2O$ = 2.11–2.98 wt%; Table 1). All samples plot in the subalkaline fields of the TAS diagram (figure not shown) and follow a typical tholeiitic trend in the $TiO_2$ versus $FeO^{total}$/MgO diagram (Fig. 9B).

The analyzed gabbros have varied levels of Cr (272–367 ppm), Ni (95–206 ppm), and V (167–260 ppm), with low total REE abundances (30–51 ppm). Chondrite-normalized patterns exhibit slight enrichment of LREEs ($[La/Yb]_N$ = 1.53–1.78) and flat HREE ($[Gd/Yb]_N$ = 1.28–1.42) patterns, with variably positive Eu anomalies (δEu = 1.11–1.31; Fig. 10E). On the primitive mantle–normalized spider diagrams, the gabbros are extremely depleted in Nb, with Nb/La ratios between 0.43 and 0.55, and variably enriched in Sr and Ba relative to their adjacent elements (Fig. 10F), resembling typical continental arc basaltic rocks (Rudnick and Gao, 2003).

## Whole-Rock Sr-Nd Isotopic Compositions

Dawan gabbros have varying $^{147}Sm/^{144}Nd$ ratios between 0.2065 and 0.2342, and $^{143}Nd/^{144}Nd$ ratios between 0.512700 and 0.513141, which correspond to a range of initial epsilon Nd ($t$ = 515 Ma) values from +0.6 to +7.4 (Fig. 11). They also show highly varied $^{87}Rb/^{86}Sr$ ratios between 0.0385 and 0.3460 and a relatively large range of $^{87}Sr/^{86}Sr$ ratios from 0.7056 to 0.7078, corresponding to initial $(^{87}Sr/^{86}Sr)_i$ ratios of 0.7046–0.7054 (Table 2). The samples from the Dabanxi intrusion show a narrow range of $^{87}Rb/^{86}Sr$ ratios (0.0932–0.1848) and $^{87}Sr/^{86}Sr$ ratios (0.7070–0.7080), as well as near-identical initial $^{87}Sr/^{86}Sr$ ratios (0.7059–0.7074). The neodymium isotopic compositions of samples from the Dabanxi intrusion have $^{147}Sm/^{144}Nd$ ratios between 0.1792 and 0.1890 and $^{143}Nd/^{144}Nd$ ratios between 0.512626 and 0.512825, with $\varepsilon_{Nd}(t)$ values from +0.6 to +4.1 (Fig. 11). Positive $\varepsilon_{Nd}(t)$ values and low $(^{87}Sr/^{86}Sr)_i$ ratios suggest that the parental magmas of the Dawan and Dabanxi gabbroic intrusions were derived from depleted mantle sources. In contrast to the gabbros, the two representative andesite samples from the lower Lapeiquan Formation have nearly constant initial $^{87}Sr/^{86}Sr$ ratios (0.7117–0.7146) and negative $\varepsilon_{Nd}(t)$ values in the range –3.7 to –5.8 (Fig. 11).

## DISCUSSION

### Depositional Age of the Lapeiquan Formation

As mentioned above, the ages of one rhyolitic sample from the lower Lapeiquan Formation and two rhyolite samples from the upper Lapeiquan

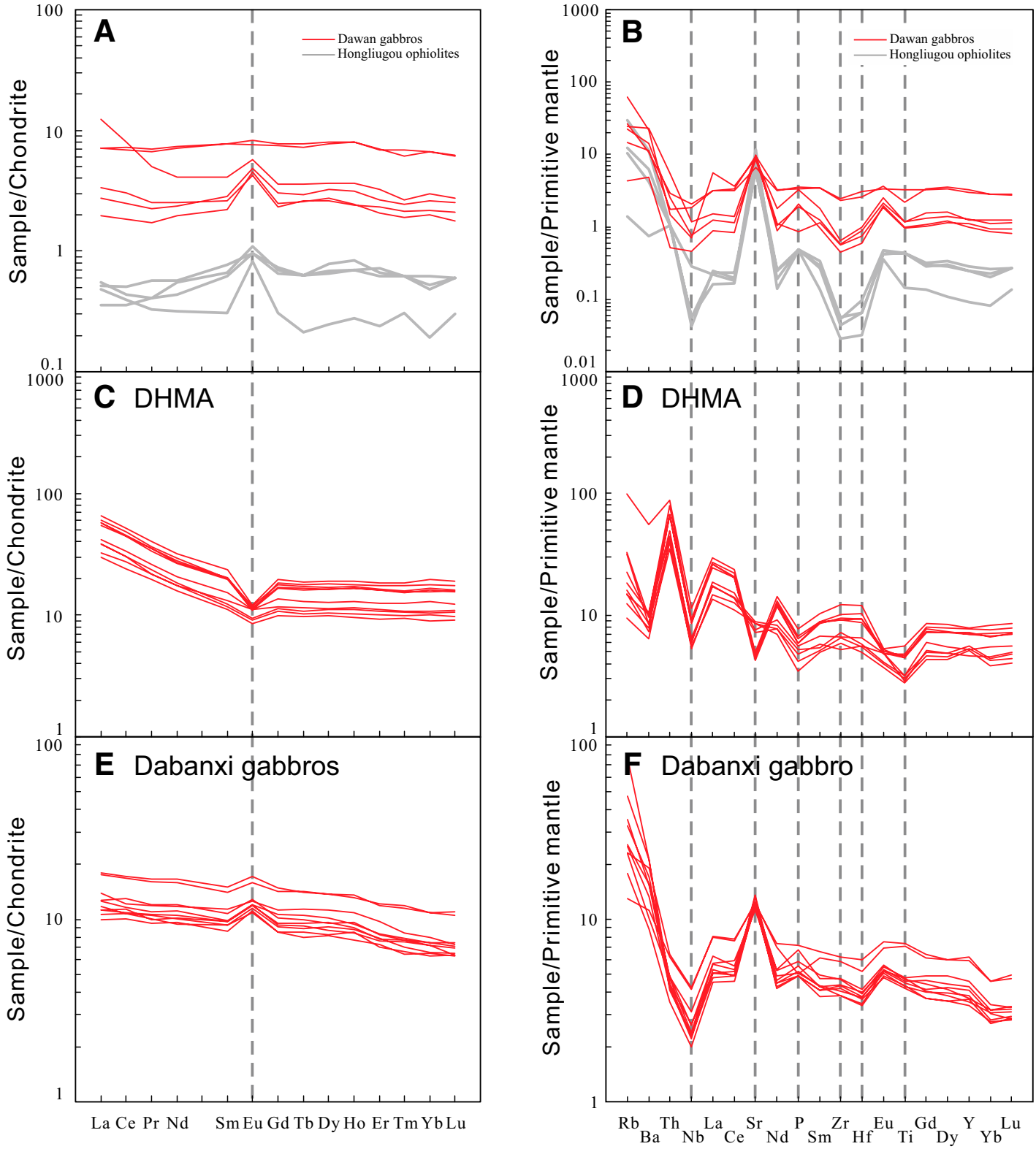


**Figure 10. Chondrite-normalized rare earth element (REE) patterns and primitive mantle–normalized trace-element spider diagrams for gabbro samples from the Dawan gabbros (A, B), Dawan andesites (C, D), and Dabanxi gabbros (E, F), respectively. Chondrite-normalizing values are from Boynton (1984), primitive mantle–normalizing values are from Sun and McDonough (1989), and the data of the Hongliugou ophiolites is from Yang et al. (2008). DHMA—Dawan high-Mg andesite.**

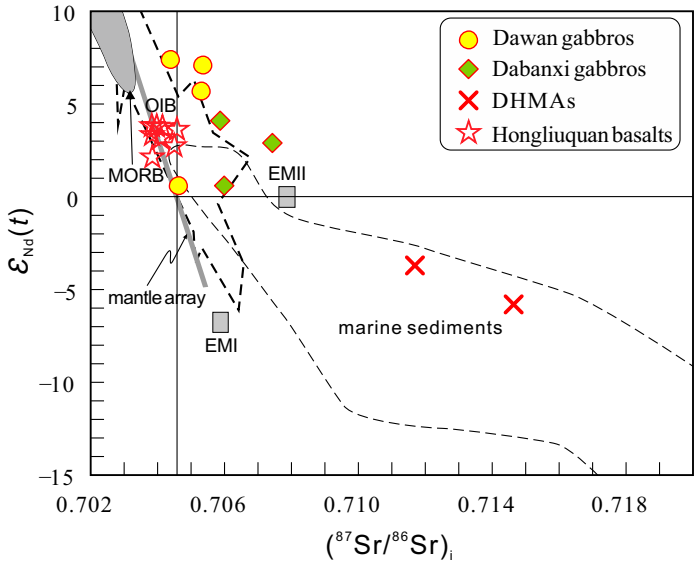


**Figure 11. Nd-Sr isotope diagrams for the Dawan gabbros, Dawan high-Mg andesites (DHMAs), and Dabanxi gabbros. Mid-ocean-ridge basalt (MORB) field is from Zimmer et al. (1995), oceanic-island basalt (OIB) field is from White and Duncan (1996), enriched mantle values (EMI and EMII) are from Hart (1988), and marine sediments are from Plank and Langmuir (1998). Data for Hongliuquan basalts are from Meng et al. (2010).**

Formation indicated that the eruption of these volcanic rocks occurred over a short interval between 495 and 485 Ma, suggesting that this volcaniclastic-sedimentary sequence was deposited during the late Cambrian rather than Mesoproterozoic Era (Xinjiang BGMR, 1981) or Ordovician Period (Xinjiang BGMR, 2006). Moreover, previous geochronological studies demonstrated that granitic plutons that intruded the Lapeiquan Formation were mostly emplaced from 490 to 420 Ma, which is consistent with the age of deposition of the Lapeiquan Formation within analytical errors. Thus, we can conclude that the Lapeiquan Formation was deposited during the late Cambrian (495–485 Ma).

## Petrogenesis

### *Dawan Gabbros*

All selected gabbros from the Dawan intrusion are characterized by a strong depletion in Nb (Fig. 10B), indicating that a continental component might have been involved in their origin, as continental crust is typically depleted in Nb (Barth et al., 2000; Rudnick and Gao, 2003). Nevertheless, the following evidence argues against significant crust incorporation into the primitive magma: (1) There is no obvious correlation between Nb/La, U/Nb, or Th/La and $SiO_2$ for the Dawan gabbros (Figs. 12A, 12B, and 12C), which contradicts the contamination model because crustal material would diminish Nb/La ratios and elevate both U/Nb and Th/La ratios at the same time. (2) Crustal contamination could simultaneously elevate La/Sm ratios and decrease $\varepsilon_{Nd}(t)$ values. However, no negative correlation between La/Sm and $\varepsilon_{Nd}(t)$ has been observed (Fig. 12D). Thus, we conclude that no significant crustal contamination occurred in the formation of the Dawan gabbros.

Due to their notably depleted Nd isotopic compositions, the Dawan gabbros are comparable to normal mid-ocean-ridge basalt (N-MORB) generated by decompression partial melting of anhydrous peridotites associated with depleted asthenospheric mantle (Hirose and Kushiro, 1993; Zindler and Hart, 1986). Furthermore, their relatively flat REE patterns also argue against an origin from partial melting of an enriched mantle wedge formed by fluid metasomatism in subduction zones. In addition, their geochemical signatures are similar to those of the Hongliugou ophiolites (Figs. 10A and 10B; Gao et al., 2012; Yang et al., 2008). Therefore, we reason that the Dawan gabbros were derived from depleted asthenospheric mantle. Nevertheless, compared to normal MORB, the Dawan gabbros exhibit significant Nb depletion on the primitive mantle–normalized diagrams, and lower Nd isotopic ratios than MORB (Figs. 10B and 11). This implies that enriched lithospheric mantle participated in the formation of the Dawan gabbros (Tang et al., 2006).

It has been demonstrated that formation of enriched lithospheric mantle can be attributed to previous melts or fluid metasomatism in ancient subduction zones (Pearce et al., 2005). Generally, slab-derived fluids are enriched in LILEs (e.g., K, Rb) and depleted in HFSEs (e.g., Nb, Ta), whereas LREEs and Th are strongly incorporated into subducted oceanic slab–derived melts (Tatsumi and Eggins, 1995; Woodhead et al., 2001). The Dawan gabbros are depleted in HFSEs and show a relatively large range of U/Th ratios (0.4–4.0), as well as low and constant Th/Nb ratios (0.11–0.55). These results imply that the lithospheric mantle had been metasomatized by ancient slab–derived hydrous fluids (Hawkesworth et al., 1993; Pearce and Peate, 1995; Saunders et al., 1991; Stern, 2002).

The Dawan gabbros show variable Mg# (72–78) and compatible elemental concentrations (e.g., Cr = 334–1080 ppm), indicating the samples underwent various degrees of fractional crystallization. Increasing CaO and $Al_2O_3$ contents with increasing Mg# indicate the fractionation of clinopyroxene (e.g., Yang and Zhou, 2009; Zhu et al., 2010), which is in agreement with the positive correlation of Cr with Mg#. On incompatible elements spider diagrams, the Dawan gabbros show positive Sr anomalies (Fig. 10B), implying accumulation of plagioclase, which is consistent with their positive Eu anomalies in the REE patterns (Fig. 10A).

### *Dawan High-Mg Andesites*

We employed Nb/La, U/Nb, and Th/La ratios as indicators to evaluate the effect of crustal contamination of mantle-derived magmas. There are near-horizontal correlation patterns in the diagrams of Nb/La-$SiO_2$, U/Nb-$SiO_2$, and Th/La-$SiO_2$ (Figs. 12A, 12B, and 12C), arguing against significant crustal contamination during magma ascent. Moreover, the $\varepsilon_{Nd}(t)$ values do not show large variations in these samples, which provide further evidence that the magmas were not notably affected by crustal materials. Thus, the geochemical characteristics of the Dawan high-Mg andesites can be used to decipher their mantle sources and the processes of their magma evolution.

Several magmatic processes has been proposed to explain the formation of high-Mg andesites, including (1) partial melting of hydrated peridotite (Kelemen, 1995; Straub et al., 2011; Tatsumi, 1981; Wood and Turner, 2009), (2) interaction between the lower crust and asthenosphere via delamination or slab breakoff (Xu et al., 2002; Gao et al., 2004; Q. Wang et al., 2006), (3) crustal-level magma mixing between crust-derived felsic and mantle-derived mafic magmas (Shellnutt and Zellmer, 2010; Streck et al., 2007), or (4) interaction between melts (slab and/or sediment) and the mantle wedge (e.g., Kelemen, 1995; X.W. Li et al., 2013; Qian et al., 2017; Tatsumi, 2001; Tsuchiya et al., 2005; Wang et al., 2011; Yogodzinski et al., 1995).

High-pressure melting experiments have illustrated that partial melting of dry refractory peridotite cannot produce a high-Mg melt (Falloon et al., 1997), while hydrous peridotite can generate high-Mg andesitic melts with relatively low levels of $TiO_2$ (0.55–0.70 wt%), $Fe_2O_3^T$ (4.04–5.36 wt%), and $Na_2O$ (1.10–3.09 wt%), as well as high concentrations of $Al_2O_3$ (17.2–21.7 wt%) and CaO (8.53–9.99 wt%; Hirose, 1997). However, the major oxides and negative Nd isotopic compositions of the Dawan

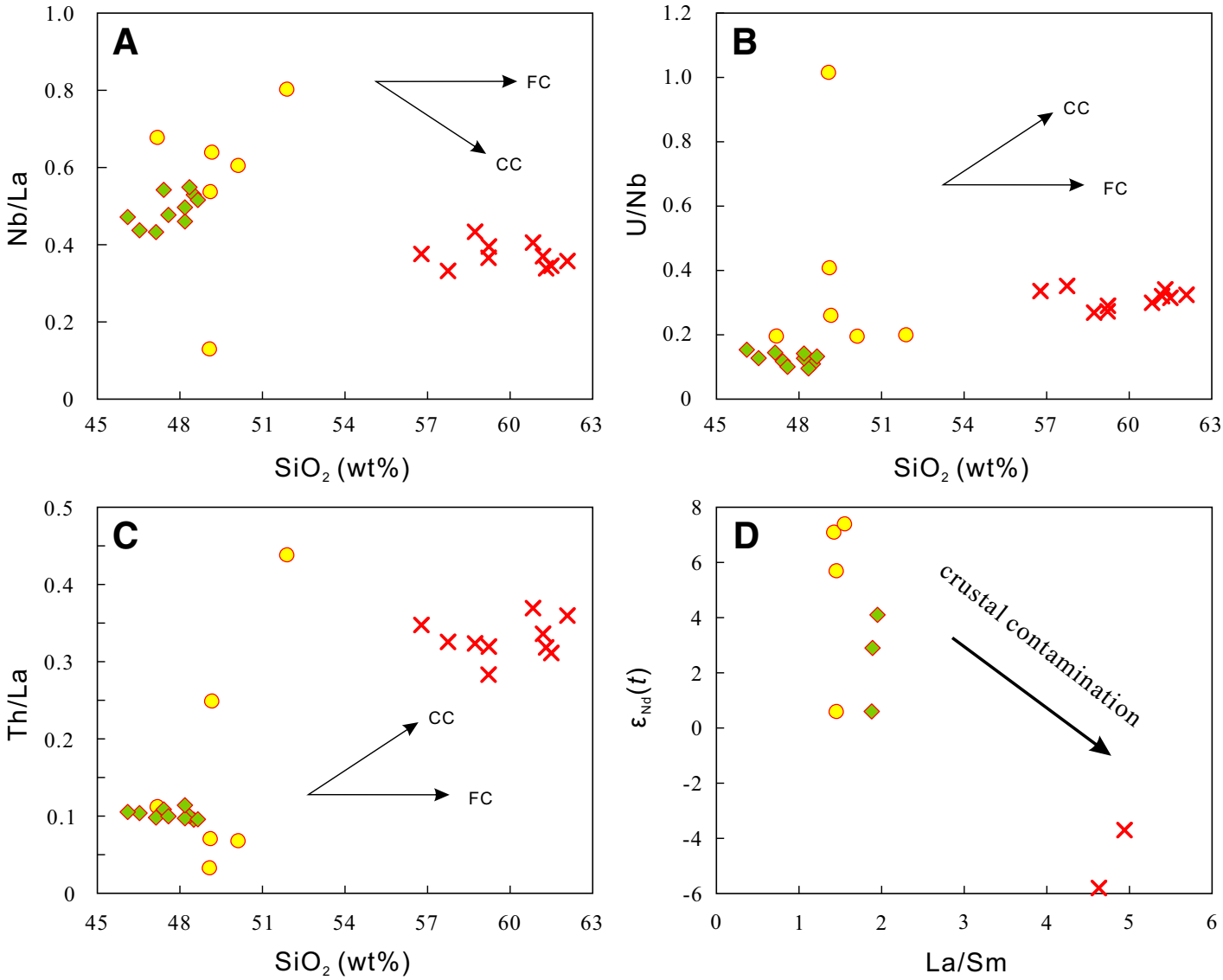


**Figure 12. (A) Nb/La vs. $SiO_2$ (wt%), (B) U/Nb vs. $SiO_2$ (wt%), (C) Th/La vs. $SiO_2$ (wt%), and (D) $\varepsilon_{Nd}(t)$ vs. La/Sm diagrams indicating crustal contamination (symbols are the same as those in Fig. 9). CC—crustal contamination, FC—fractional crystallization.**

high-Mg andesites readily rule out the first model. Instead, andesitic melts, which are genetically related to the foundering of mafic lower crust into the underlying asthenospheric mantle followed by immediate partial melting, will produce the depleted signatures (Gao et al., 2004; Qin et al., 2010). Furthermore, partial melting of lower crust generates high-Mg adakitic magma with high Sr (>400 ppm) and Sr/Y (>20), low Y (<18 ppm) and Yb (<1.9 ppm), and high LREE/HREE ratios with $(La/Yb)_N > 20$ (e.g., X.R. Wang et al., 2006; Tang and Wang, 2010; Wang et al., 2008). However, the enriched Nd isotopic compositions and relative low Sr (89.5–186 ppm) and high Y (21.1–35.4 ppm) and Yb (2.09–4.09 ppm) contents of the Dawan high-Mg andesites contradict this model. The magma mixing model would show variable isotopic and geochemical signatures. However, rhyolites in the upper Lapeiquan Formation have positive $\varepsilon_{Nd}(t)$ and zircon $\varepsilon_{Hf}(t)$ values (our unpublished data). Moreover, the absence of contemporaneous mafic rocks in this area also rules out the mixing model. Thus, these first three models do not sufficiently explain the formation of the Dawan high-Mg andesites.

As an alternative, we favor the fourth model, which postulates the formation of the Dawan high-Mg andesites by interaction between mantle peridotite and sediment-derived melts. First, the Dawan high-Mg andesites show relatively high MgO and Cr contents, indicating partial melting of a refractory mantle source that previously underwent extraction of basaltic melt (e.g., Yogodzinski et al., 1995; Zhang et al., 2012). Second, the Dawan high-Mg andesites show low $\varepsilon_{Nd}(t)$ values, high Th/La and Th/Nb ratios, and low Nb/Ta ratios, similar to those of marine sediments or upper continental crust. The Dawan high-Mg andesites share geochemical features similar to sanukitoids in the Japan arc, which are considered to have been generated by the interaction of subducted oceanic sediment–derived melts and mantle peridotites (Shimoda et al., 1998; Tatsumi, 2001; Tatsumi and Hanyu, 2003; Wang et al., 2011). Furthermore, the Dawan high-Mg andesites have relatively restricted and high Th/Nb ratios (0.75–1.01) and low U/Th ratios (0.32–0.36), which provide further evidence for the involvement of a sediment-derived component rather than slab-derived fluids. Based on these considerations, we argue that the Dawan high-Mg

andesites were likely generated by interaction between sediment-derived melts and basaltic melts originating from mantle wedge peridotites.

### *Dabanxi Intrusion*

The Dabanxi gabbroic rocks show significant Nb depletion on primitive mantle–normalized diagrams, and all samples exhibit slight LREE enrichment, implying possible involvement of a continental component in their origin. Nevertheless, the following evidence rules out the possibility of significant crustal component involvement in their origin: (1) The analyzed samples show a wide range of $SiO_2$ contents but relatively constant Nb/La (0.43–0.55), U/Nb (0.10–0.15), and Th/La (0.10–0.11) ratios (Figs. 12A, 12B, and 12C); (2) crustal contamination could simultaneously elevate La/Sm ratios and decrease $\varepsilon_{Nd}(t)$ values; however, such a trend was not observed in the samples (Fig. 12D); and (3) no xenocrystic zircon indicative of crustal contamination was detected by CL imaging and SHRIMP zircon U-Pb dating.

Thus, we conclude that the parent magma of the Dabanxi intrusion reflects metasomatism of the mantle source, rather than crustal contamination. The large variation in Nd isotopic compositions might have resulted from the heterogeneity of the mantle source. In the Th/Nb versus U/Th diagram (Fig. 13), the Dabanxi gabbros show a wide distribution of U/Th ratios (0.48–0.71) with a narrow range of relatively low Th/Nb ratios (0.18–0.24), suggesting that the parental magma was probably derived from a mantle source modified by hydrous fluids rather than sediments (Hawkesworth et al., 1997; Pearce and Peate, 1995; Saunders et al., 1991; Stern, 2002).

The mantle wedge above the subduction zone can be modified by fluids derived from dehydration of altered oceanic crust (Hawkesworth et al., 1993; Turner et al., 1997). The fluids could not only modify the mantle composition, but also lower the solidus curve of the mantle (e.g., Yang and Zhou, 2009). The Dabanxi gabbros exhibit enrichment of LREEs (Fig. 10E) and depletion of HFSEs with high LREE/HFSE ratios (e.g., La/Nb). In addition, the clinopyroxenes from the Dabanxi gabbros are characterized by high $Al_2O_3$ and low $Cr_2O_3$ and $TiO_2$ contents (Fig. 14B). This suggests that the Dabanxi intrusion formed in a subduction-related environment. The primitive magmas were likely derived from a mantle wedge modified by slab-derived fluids.

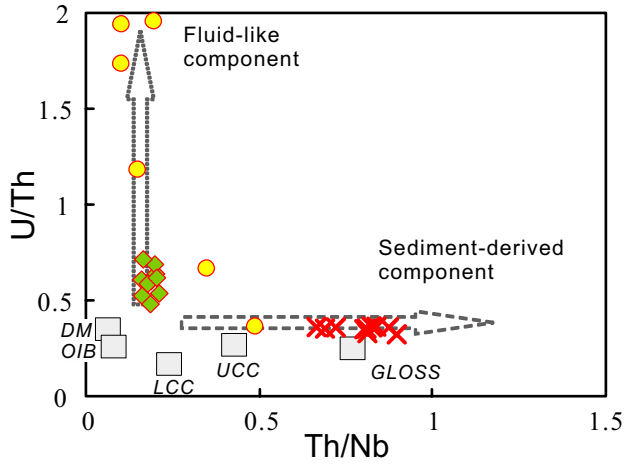


**Figure 13. U/Th vs. Th/Nb diagrams for gabbros and andesites (symbols are the same as those in Fig. 9). DM—depleted mantle; OIB—oceanic-island basalt; LCC—lower continental crust; UCC—upper continental crust; GLOSS—global subducting sediment.**

As for the gabbros from the Dabanxi intrusion, the correlations of CaO, $Al_2O_3$, and Cr with Mg# are similar to the Dawan gabbros, suggesting that clinopyroxene also was a significant fractionating mineral in the magma evolution process. Positive Eu and Sr anomalies reveal the accumulation of plagioclase (Figs. 10E and 10F). Therefore, the Dabanxi gabbros were likely formed by mantle wedge–derived melts, which then underwent fractional crystallization during magma ascent.

## Tectonic Implications

Numerous investigations have been carried out in the last few decades in the Altun orogenic belt (e.g., Chen et al., 2003, 2009; Y.B. Gao et al., 2011; X.F. Gao et al., 2012; Han et al., 2012; S.B. Li et al., 2013; Qi et al., 2005a, 2005b; Sun et al., 2012; Wu et al., 2006; Z.C. Zhang et al., 2010).

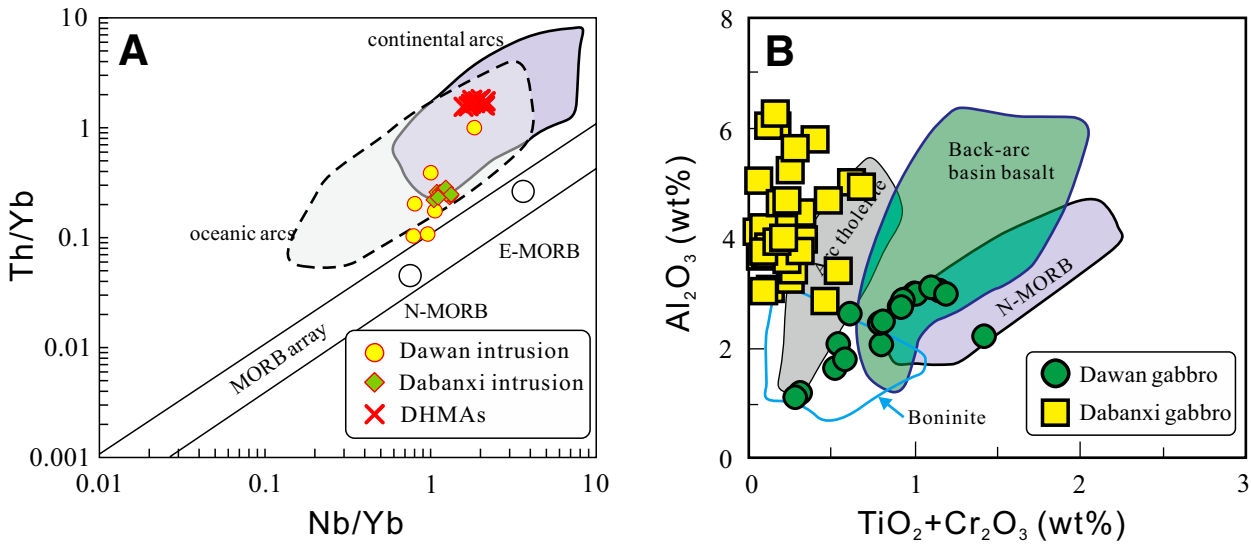


**Figure 14. (A) Th/Yb vs. Nb/Yb diagram for gabbros and andesites (modified from Pearce, 2014; symbols are the same as those in Fig. 9). (B) $Al_2O_3$ (wt%) vs. ($TiO_2$ + $Cr_2O_3$) (wt%) diagram of clinopyroxene from the gabbro of the Dawan and Dabanxi mafic intrusions. DHMAs—Dawan high-Mg andesites; MORB—mid-ocean-ridge basalt (E—enriched, N—normal).**

These studies have identified two ophiolite zones (Hongliugou-Lapeiquan and south Altun) in the Altun orogenic belt and have demonstrated the existence of the North and South Altun Oceans (L. Liu et al., 1997, 2012). It is considered that the North Altun Ocean basin opened ca. 750 Ma (H. Liu et al., 2012) and then started to subduct from 520 to 500 Ma (Han et al., 2012; Kang et al., 2011; C. Liu et al., 2016; Wu et al., 2009), and then the subduction angle changed (e.g., slab rollback and flat-slab subduction) during 520–460 Ma, and it was completely closed by ca. 450 Ma (Hao et al., 2006). The existence of volcanic-arc granites on both sides of the Hongliugou-Lapeiquan ophiolite belt suggests that the oceanic lithosphere might have undergone divergent double-sided subduction (C. Liu et al., 2016; J.H. Liu et al., 2017). However, the petrogenesis of the Dawan gabbros and the Dawan high-Mg andesites cannot be sufficiently explained by a normal oceanic subduction event. These rocks were generally related to upwelling of asthenospheric mantle. Three competing mechanisms should be taken into account: (1) ocean-ridge subduction (e.g., Cai et al., 2012; Dickinson and Snyder, 1979; Windley et al., 2007; Sun et al., 2009; Zhang et al., 2014), (2) slab breakoff (e.g., Atherton and Ghani, 2002; Davies and von Blanckenburg, 1995; Niu et al., 2006; van Hunen and Allen, 2011), and (3) slab rollback (Hawkins et al., 1990; Xu et al., 2003; Yan et al., 2016).

Ocean-ridge subduction causes voluminous magmatic activity and HT/LP metamorphism (Kusky et al., 2003; Sisson et al., 2003; Windley et al., 2007). Ridge subduction is responsible for the formation of a slab window, which induces upwelling of hot and depleted asthenospheric mantle. This process generally accounts for the origination of MORB-like adakitic and boninitic rocks (Sisson et al., 2003). Recent studies indicate that the circum-Pacific regions have been affected by ridge subduction in the formation of the accretionary orogens in Japan, Alaska, and Chile (Cai et al., 2012, and references therein). Also, ridge subduction has been invoked in several regions of the Central Asian orogenic belt (e.g., West Junggar, Chinese Altai, and Inner Mongolia; Cai et al., 2012; Geng et al., 2009; Sun et al., 2009). However, the lack of coeval adakites and boninites in the North Altun clearly contradicts the ocean-ridge subduction model. Furthermore, there is no evidence for any high-temperature metamorphic events in this tectonic belt. These findings prompted us to rule out the possibility of ridge subduction during the Cambrian.

Slab breakoff associated with the final detachment of a lithospheric slab (Davies and von Blanckenburg, 1995; Xu et al., 2008) has been proposed as an explanation of the distinct igneous activity during the early stages of continent-continent or continent-arc collision (Atherton and Ghani, 2002; Davies and von Blanckenburg, 1995; Teng et al., 2000; Zhu et al., 2015). However, there is no evidence suggesting the occurrence of early Cambrian (ca. 520 Ma) collision in the North Altun. Instead, the subduction process most likely lasted until ca. 460 Ma in this area (Chen et al., 2016; Cui et al., 2010; Han et al., 2012; S.B. Li et al., 2013; Wu et al., 2016). Thus, the slab breakoff model cannot satisfactorily describe the origin of the Dawan gabbros and the Dawan high-Mg andesites.

Alternatively, it has been suggested that slab rollback played a key role in the generation of these temporally and spatially related igneous rocks. Rollback of the subducting slab would result in extension of the arc lithosphere (Gueguen et al., 1997), which is an important driving force of back-arc basin formation (Nakakuki and Mura, 2013). Partial melting of the upwelling asthenospheric mantle beneath an ocean-ridge system in a suprasubduction zone induces the formation of back-arc basin basalts, most of which show volcanic arc-like and MORB-like compositional characteristics (Evans et al., 1991; Hawkins et al., 1990; Xu et al., 2003).

The Dawan gabbros show varying extents of depletion or enrichment of LREEs and have high $\varepsilon_{Nd}(t)$ values, indicating that a component from depleted asthenospheric mantle was involved in their generation. However, all these gabbros plot between the MORB array and the field of arc-like volcanics (Fig. 14A). Furthermore, the clinopyroxenes from the Dawan gabbros exhibit arc-related trends and plot in the overlapping area between normal MORB and back-arc basin basalt (Figs. 8C and 14B). These observations strongly argue that the Dawan gabbros share a systematic back-arc basin basalt compositional signature and that they were most probably formed in a back-arc basin environment, in apparent consistency with the slab rollback model. In this scenario, the migration of the subducting slab backward into the asthenospheric mantle (rollback) results in the upwelling and decompression melting of hot asthenospheric mantle. This process is followed by partial melting of the subcontinental lithospheric mantle, which ultimately leads to the formation of the parental Dawan gabbro melt. Asthenospheric upwelling results in high-temperature conditions that reheat the cooled subducted slab, subsequently causing sediment melting. These sediment-derived melts react with the mantle wedge and result in partial melting of the metasomatized mantle peridotites, generating magmas like the Dawan high-Mg andesite magmas. Thus, we argue that the slab rollback (formation of back-arc basin) model is also consistent with the formation of the slightly younger Dawan high-Mg andesites.

Previous studies have provided abundant evidence in support of the hypothesis that the North Altun is the western extension of the North Qilian, separated into two parts by the Altyn Tagh fault. Based on identification of a HP/LT metamorphic belt, ophiolites, a subduction-accretion complex, and arc magmatic rocks, the North Altun is considered to be an early Paleozoic accretionary orogen, recognized as the northernmost orogenic collage of the proto-Tethyan domain (Li et al., 2017; Zhang et al., 2015, 2017). The initial rifting of the North Altun Ocean (proto-Tethys) began around ca. 750 Ma, according to the ages of bimodal volcanics identified in the North Altun (H. Liu et al., 2012). Though the exact timing of the initial subduction is unknown, the ocean basin already existed during the early–late Cambrian, as indicated by the ages of the gabbro (480 Ma; Yang et al., 2008) and of the plagiogranite (518–512 Ma; Gai et al., 2015; Gao et al., 2012) from the Hongliugou ophiolitic mélange. From ca. 520 to 495 Ma, oceanic slab rollback induced back-arc extension and resulted in upwelling of the asthenospheric mantle. Dawan gabbro magmas and Dawan high-Mg andesites were generated at the back-arc and the forearc, respectively (Fig. 15A). From the late Cambrian (490 Ma) to the Middle Ordovician (460 Ma), during the subduction of the North Altun Ocean, hydrous fluids released from the slab metasomatized the refractory mantle wedge. The addition of water caused the mantle wedge to be partially melted. Basaltic underplating provided the heat necessary for the melting of the lower and middle crust, which was followed by the generation of arc-related voluminous felsic magmas in the North Altun (Fig. 15B; e.g., Chen et al., 2016; Cui et al., 2010; Han et al., 2012; S.B. Li et al., 2013; Wu et al., 2016).

## CONCLUSIONS

(1) Zircon U-Pb dating from rhyolite interbedded in the Lapeiquan Formation shows that the Lapeiquan volcanic-sedimentary sequence was deposited during the late Cambrian (495–485 Ma).

(2) The Dawan gabbro melts were generated from the asthenosphere with variable degrees of contribution from the lithospheric mantle. Dawan high-Mg andesites originated from the subsequent interaction between sediment-derived melts and mantle wedge peridotites. The Dabanxi gabbros were derived from the mantle wedge, which was metasomatized by fluids released from the subducted slab.

(3) The slab rollback model provides a satisfactory explanation of how the Dawan gabbros and the Dawan high-Mg andesites were formed in the North Altun, as the subduction of the North Altun Ocean might have lasted until ca. 460 Ma.

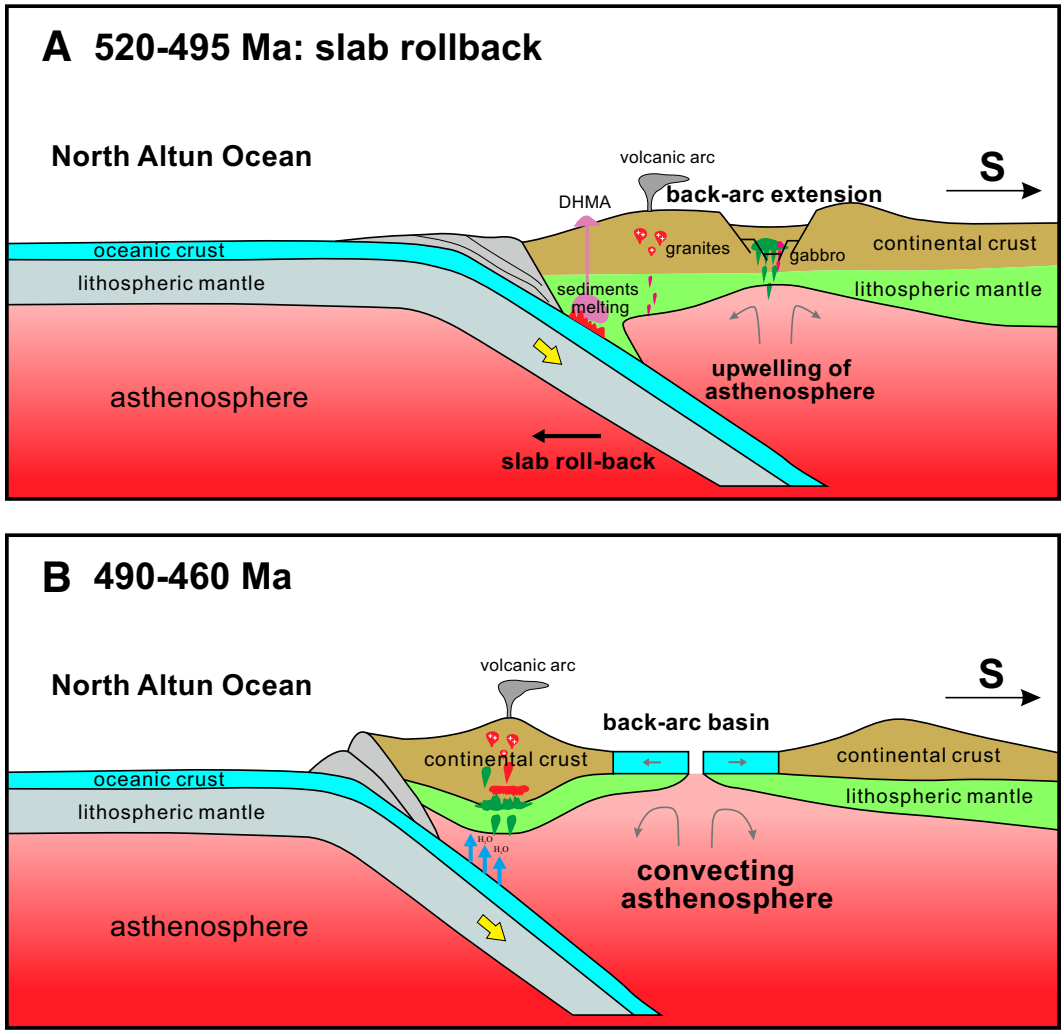


**Figure 15. Cartoon model illustrating the formation of the Dawan gabbros, Dawan andesites, and Dabanxi gabbros (see details in the text). DHMA—Dawan high-Mg andesite.**


## ACKNOWLEDGMENTS

This work was supported by the National Natural Science Foundation of China (41702197), the Natural Science Foundation of Jiangsu Province of China (BK20170873), and the Fundamental Research Funds for the Central Universities (2017B03614). We appreciate the help of Hang-Qiang Xie, Jian-Zhen Geng, and Jian Zhang with zircon sensitive high-resolution ion microprobe (SHRIMP) and laser-ablation-inductively coupled plasma-mass spectrometry (LA-ICP-MS) U-Pb age dating, Guo-Lin Guo with mineral chemical composition analyses, and Jing Hu and Liang Qi with trace-element and Sr-Nd isotope analyses. R. Damian Nance and four anonymous reviewers are acknowledged for their constructive comments.


## REFERENCES CITED


Atherton, M.P., and Ghani, A.A., 2002, Slab breakoff: A model for Caledonian, Late Granite syn-collisional magmatism in the orthotectonic (metamorphic) zone of Scotland and Donegal, Ireland: Lithos, v. 62, p. 65–85, https://doi.org/10.1016/S0024-4937(02)00111-1.

Barth, M.G., McDonough, W.F., and Rudnick, R.L., 2000, Tracking the budget of Nb and Ta in the continental crust: Chemical Geology, v. 165, p. 197–213, https://doi.org/10.1016/S0009-2541(99)00173-4.

Boynton, W.V., 1984, Geochemistry of the rare earth elements: meteorite studies, *in* Henderson, P., ed., Rare Earth Element Geochemistry: Amsterdam, Netherlands, Elsevier, p. 63–114.

Burtman, V.S., and Molnar, P., 1993, Geological and Geophysical Evidence for Deep Subduction of Continental Crust Beneath the Pamir: Geological Society of America Special Paper 281, 76 p., https://doi.org/10.1130/spe281-p1.

Cai, K.D., Sun, M., Yuan, C., Zhao, G.C., Xiao, W.J., and Long, X.P., 2012, Keketuohai mafic-ultramafic complex in the Chinese Altai, NW China: Petrogenesis and geodynamic significance: Chemical Geology, v. 294, p. 26–41, https://doi.org/10.1016/j.chemgeo.2011.11.031.

Che, Z.C., Liu, L., Liu, H.F., and Luo, J.H., 1995, Discovery and occurrence of high-pressure metapelitic rocks from Altun Mountain areas, Xinjiang Autonomous Region: Chinese Science Bulletin, v. 40, p. 1988–1991 [in Chinese with English abstract].

Chen, B.L., Li, S.B., Jiang, R.B., Chen, Z.L., Han, F.B., Cui, L.L., Li, L., Zhao, S.M., Qi, W.X., Yang, Y., Wang, S.X., Wang, Y., Zhou, Y.G., and Hao, R.X., 2016, Zircon SHRIMP U-Pb dating of intermediate-felsic volcanic rocks from the Kaladawan area, Altun Mountains, and its tectonic environment: Acta Geologica Sinica, v. 90, p. 708–727 [in Chinese with English abstract].

Chen, X.H., George, G., Wang, X.F., Yang, F., and Chen, Z.L., 2003, Granite from North Altun Tagh, NW China: U-Pb geochronology and tectonic setting: Bulletin of Mineralogy, Petrology and Geochemistry, v. 22, p. 294–298 [in Chinese with English abstract].

Chen, X.H., Yin, A., Gehrels, G.E., Jiang, R.B., Chen, Z.L., and Bai, Y.F., 2009, Geothermochronology and tectonic evolution of the Eastern Altun Tagh Mountains, northwestern China: Earth Science Frontiers, v. 16, p. 207–219 [in Chinese with English abstract].

Cowgill, E., Yin, A., Harrison, T.M., and Wang, X.F., 2003, Reconstruction of the Altun Tagh fault based on U-Pb geochronology: Role of back thrusts, mantle sutures, and heterogeneous crustal strength in forming the Tibetan Plateau: Journal of Geophysical Research–Solid Earth (1978–2012), v. 108, no. B7, 2346, https://doi.org/10.1029/2002JB002080

Cui, L.L., Chen, B.L., Yang, N., Chen, Z.L., and Ding, W.J., 2010, Geochemistry and genesis of basic-intermediate volcanic rocks from Kaladawan, east Altun Tagh Mountains: Journal of Geometry, v. 16, p. 96–107 [in Chinese with English abstract].

Davies, J.H., and von Blanckenburg, F., 1995, Slab breakoff: A model of lithosphere detachment and its test in the magmatism and deformation of collisional orogens: Earth and Planetary Science Letters, v. 129, p. 85–102, https://doi.org/10.1016/0012-821x(94)00237-s.

DePaolo, D.J., 1981, Trace element and isotopic effects of combined wall rock assimilation and fractional crystallization: Earth and Planetary Science Letters, v. 53, p. 189–202, https://doi.org/10.1016/0012-821X(81)90153-9.

Dickinson, W.R., and Snyder, W.S., 1979, Geometry of triple junctions related to San Andreas transform: Journal of Geophysical Research–Solid Earth, v. 84, p. 561–572, https://doi.org/10.1029/JB084iB02p00561.

Dong, S.L., Li, Z., Gao, J., and Zhu, L., 2013, Progress of studies on early Paleozoic tectonic framework and crystalline rock geochronology in Altun-Qilian-Kunlun orogen: Geological Review, v. 59, p. 731–746 [in Chinese with English abstract].

Evans, C.A., Castaněda, G., and Franco, H., 1991, Geochemical complexities preserved in the volcanic rocks of the Zambales ophiolite, Philippines: Journal of Geophysical Research–Solid Earth, v. 96, p. 16,251–16,262, https://doi.org/10.1029/91JB01488.

Falloon, T.J., Green, D.H., O'Neill, H.S.C., and Hibberson, W.O., 1997, Experimental tests of low degree peridotite partial melt compositions: Implications for the nature of anhydrous near-solidus peridotite melts at 1 GPa: Earth and Planetary Science Letters, v. 152, p. 149–162, https://doi.org/10.1016/S0012-821X(97)00155-6.

Fan, H.P., Zhu, W.G., Li, Z.X., Zhong, H., Bai, Z.J., He, D.F., Chen, C.J., and Cao, C.Y., 2013, Ca. 1.5 Ga mafic magmatism in South China during the break-up of the supercontinent Nuna/Columbia: The Zhuqing Fe-Ti-V oxide ore-bearing mafic intrusions in western Yangtze block: Lithos, v. 168, p. 85–98, https://doi.org/10.1016/j.lithos.2013.02.004.

Gai, Y.S., Liu, L., Kang, L., Yang, W.Q., Liao, X.Y., and Wang, Y.W., 2015, The origin and geologic significance of plagiogranite in the ophiolite belt at North Altun Tagh: Acta Petrologica Sinica, v. 31, p. 2549–2565 [in Chinese with English abstract].

Gao, S., Rudnick, R.L., Yuan, H.L., Liu, X.M., Liu, Y.S., Xu, W.L., Ling, W.L., Ayers, J., Wang, X.C., and Wang, Q.H., 2004, Recycling lower continental crust in the North China craton: Nature, v. 432, p. 892–897, https://doi.org/10.1038/nature03162.

Gao, X.F., Xiao, P.X., Guo, L., Dong, Z.C., and Xi, R.G., 2012, Opening of an early Paleozoic limited oceanic basin in the northern Altun area: Constraints from plagiogranites in the Hongliugou-Lapeiquan ophiolitic mélange: Science China–Earth Sciences, v. 42, p. 359–368 [in Chinese].

Gao, Y.B., Li, W.Y., Li, K., Zhang, Z.W., and Zhang, J.W., 2011, Geological and geochemical characteristics of intermediate-acid intrusive rocks in Altun and east Kunlun orogenic belt and their significances: Xinjiang Geology, v. 29, p. 359–366 [in Chinese with English abstract].

Gehrels, G.E., Yin, A., and Wang, X.F., 2003, Detrital-zircon geochronology of the northeastern Tibetan Plateau: Geological Society of America Bulletin, v. 115, p. 881–896, https://doi.org/10.1130/0016-7606(2003)115<0881:DGOTNT>2.0.CO;2.

Geng, H.Y., Sun, M., Yuan, C., Xiao, W.J., Xian, W.S., Zhao, G.C., Zhang, L.F., Wong, K., and Wu, F.Y., 2009, Geochemical, Sr-Nd and zircon U-Pb-Hf isotopic studies of late Carboniferous magmatism in the West Junggar, Xinjiang: Implications for ridge subduction: Chemical Geology, v. 266, p. 364–389, https://doi.org/10.1016/j.chemgeo.2009.07.001.

Geng, J.Z., Li, H.K., Zhang, J., and Zhang, Y.Q., 2011, Zircon Hf isotope analysis by means of LA-MC-ICP-MS: Geological Bulletin of China, v. 30, p. 1508–1513 [in Chinese with English abstract].

Gueguen, E., Doglioni, C., and Fernandez, M., 1997, Lithospheric boudinage in the Western Mediterranean back-arc basin: Terra Nova, v. 9, p. 184–187, https://doi.org/10.1046/j.1365-3121.1997.d01-28.x.

Guo, Z.J., Zhang, Z.C., and Wang, J.J., 1998, Sm-Nd isochron age and tectonic significance of ophiolite complex in the North Altun Mountains: Chinese Science Bulletin, v. 43, p. 1981–1984 [in Chinese with English abstract].

Han, F.B., Chen, B.L., Cui, L.L., Wang, S.X., Chen, Z.L., Jiang, R.B., Li, L., and Qi, W.X., 2012, Zircon SHRIMP U-Pb ages of intermediate-acid intrusive rocks in Kaladawan area, eastern Altun Mountains, NW China, and its implications: Acta Petrologica Sinica, v. 28, p. 2277–2291 [in Chinese with English abstract].

Hao, J., Wang, E.Q., Liu, X.H., and Sang, H.Q., 2006, Jinyanshan collision orogenic belt of the early Paleozoic in the Altun Mountains: Evidence from single zircon U-Pb and $^{40}Ar$-$^{39}Ar$ isotopic dating for the arc magmatic rocks and ophiolitic mélange: Acta Petrologica Sinica, v. 22, p. 2743–2752 [in Chinese with English abstract].

Hart, S.R., 1988, Heterogeneous mantle domains: Signature, genesis and mixing chronologies: Earth and Planetary Science Letters, v. 90, p. 273–296, https://doi.org/10.1016/0012-821X(88)90131-8.

Hawkesworth, C., Gallagher, K., Hergt, J.M., and McDermott, F., 1993, Mantle and slab contributions in arc magma: Annual Review of Earth and Planetary Sciences, v. 21, p. 175–204, https://doi.org/10.1146/annurev.ea.21.050193.001135.

Hawkesworth, C., Turner, S., Peate, D., McDermott, F., and Calsteren, P., 1997, Elemental U and Th variations in island arc rocks: Implications for U-series isotopes: Chemical Geology, v. 139, p. 207–221, https://doi.org/10.1016/S0009-2541(97)00036-3.

Hawkins, J.W., Lonsdale, P.F., Macdougall, J.D., and Volpe, A.M., 1990, Petrology of the axial ridge of the Mariana Trough backarc spreading center: Earth and Planetary Science Letters, v. 100, p. 226–250, https://doi.org/10.1016/0012-821X(90)90187-3.

Helmy, H.M., and El Mahallawi, M.M., 2003, Gabbro Akarem mafic-ultramafic complex, Eastern Desert, Egypt: A late Precambrian analogue of Alaskan-type complexes: Mineralogy and Petrology, v. 77, p. 85–108, https://doi.org/10.1007/s00710-001-0185-9.

Hirose, K., 1997, Melting experiments on lherzolite KLB-1 under hydrous conditions and generation of high-magnesian andesitic melts: Geology, v. 25, p. 42–44, https://doi.org/10.1130/0091-7613(1997)025<0042:MEOLKU>2.3.CO;2.

Hirose, K., and Kushiro, I., 1993, Partial melting of dry peridotites at high pressures: Determination of compositions of melts segregated from peridotite using aggregates of diamond: Earth and Planetary Science Letters, v. 114, p. 477–489, https://doi.org/10.1016/0012-821X(93)90077-M.

Hollanda, M.H.B.M., Pimentel, M.M., Oliveira, D.C., and Sa, E.F.J., 2006, Lithosphere-asthenosphere interaction and the origin of Cretaceous tholeiitic magmatism in northeastern Brazil: Sr-Nd-Pb isotopic evidence: Lithos, v. 86, p. 34–49, https://doi.org/10.1016/j.lithos.2005.04.004.

Hou, K.J., Li, Y.H., and Tian, Y.R., 2009, In situ U-Pb zircon dating using laser ablation–multi ion counting ICP-MS: Mineralium Deposita, v. 28, p. 481–492 [in Chinese with English abstract].

Jahn, B.M., Wu, F.Y., Lo, C.H., and Tsai, C.H., 1999, Crust-mantle interaction induced by deep subduction of the continental crust: geochemical and Sr-Nd isotopic evidence from post-collisional mafic-ultramafic intrusions of the northern Dabie complex, central China: Chemical Geology, v. 157, p. 119–146, https://doi.org/10.1016/S0009-2541(98)00197-1.

Kang, L., Liu, L., Cao, Y.T., Wang, C., Yang, W.Q., and Zhu, X.H., 2011, Geochemistry, zircon LA-ICP-MS U-Pb ages and Hf isotopes of Hongliugou moyite from North Altun Tagh tectonic belt: Geological Bulletin of China, v. 30, p. 1066–1076 [in Chinese with English abstract].

Kelemen, P.B., 1995, Genesis of high Mg andesites and the continental crust: Contributions to Mineralogy and Petrology, v. 120, p. 1–19, https://doi.org/10.1007/BF00311004.

Kepezhinskas, P., McDermott, F., Defant, M., Hochstaedter, A., Drummond, M.S., Hawdesworth, C.J., Koloskov, A., Maury, R.C., and Bellon, H., 1997, Trace element and Sr-Nd-Pb isotopic constraints on a three-component model of Kamchatka arc petrogenesis: Geochimica et Cosmochimica Acta, v. 61, p. 577–600, https://doi.org/10.1016/S0016-7037(96)00349-3.

Kusky, T.M., Bradley, D., Donley, D.T., Rowley, D., and Haeussler, P.J., 2003, Controls on intrusion of near-trench magmas of the Sanak-Baranof belt, Alaska, during Paleogene ridge subduction, and consequences for forearc evolution, *in* Sisson, V.B., Roeske, S.M., and Pavlis, T.L., eds., Geology of a Transpressional Orogen Developed During Ridge–Trench Interaction along the North Pacific Margin: Geological Society of America Special Paper 371, p. 269–292, https://doi.org/10.1130/0-8137-2371-X.269.

Li, S.B., Chen, B.L., Chen, Z.L., Hao, R.X., Zhou, Y.G., and Han, F.B., 2013, Geochemistry and tectonic implications of the early Paleozoic felsic to intermediate volcanic rocks from Kaladawan area, North Altun: Geological Review, v. 59, p. 423–436 [in Chinese with English abstract].

Li, S.Z., Zhao, S.J., Liu, X., Cao, H., Yu, S., Li, X.Y., Somerville, I., and Yu, S.Y., 2017, Closure of the proto–Tethys Ocean and early Paleozoic amalgamation of microcontinental blocks in East Asia: Earth-Science Reviews (in press), https://doi.org/10.1016/j.earscirev.2017.01.011.

Li, X.H., Liu, D.Y., Sun, M., Li, W.X., Liang, X.R., and Liu, Y., 2004, Precise Sm-Nd and U-Pb isotopic dating of the super-giant Shizhuyuan polymetallic deposit and its host granite: Southeast China: Geological Magazine, v. 141, p. 225–231, https://doi.org/10.1017/s0016756803008823.

Li, X.W., Mo, X.X., Yu, X.H., Ding, Y., Huang, X.F., Wei, P., and He, W.Y., 2013, Petrology and geochemistry of the early Mesozoic pyroxene andesites in the Maixiu area, west Qinling, China: Products of subduction or syn-collision: Lithos, v. 172–173, p. 158–174, https://doi.org/10.1016/j.lithos.2013.04.010.

Liu, C., Wu, C., Gao, Y., Lei, M., and Qin, H., 2016, Age, composition, and tectonic significance of Palaeozoic granites in the Altun orogenic belt, China: International Geology Review, v. 58, p. 131–154, https://doi.org/10.1080/00206814.2015.1056757.

Liu, H., Wang, G.C., Cao, S.Z., Luo, Y.J., Gao, R., and Huang, W.X., 2012, Discovery of Nanhuanian bimodal volcanics in northern Altun Tagh and its tectonic significance: Earth Science, v. 37, p. 917–928 [in Chinese with English abstract].

Liu, J.H., Liu, L., Gai, Y.S., Kang, L., Yang, W.Q., Liao, X.Y., and Yang, M., 2017, Zircon U-Pb dating and Hf isotopic compositions of the Baijianshan granodiorite in North Altun Tagh and its geological significance: Acta Geologica Sinica, v. 91, p. 1022–1038 [in Chinese with English abstract].

Liu, L., Che, Z., Luo, J., Wang, Y., and Gao, Z., 1997, Recognition and implication of eclogite in the western Altun Mountains, Xinjiang: Chinese Science Bulletin, v. 42, p. 931–934, https://doi.org/10.1007/BF02882551.

Liu, L., Sun, Y., Xiao, P.X., Chen, Z.C., Luo, J.H., Chen, D.L., Wang, Y., and Zhang, A.D., 2002, Discovery of ultrahigh-pressure magnesite-bearing garnet lherzolite (>3.8 GPa) in the Altyn Tagh, Northwest China: Chinese Science Bulletin, v. 47, p. 881–886, https://doi.org/10.1360/02tb9197.

Liu, L., Zhang, J.F., Green, H.W., II, Jin, Z.M., and Bozhilov, K.N., 2007, Evidence of former stishovite in metamorphosed sediments, implying subduction to >350 km: Earth and Planetary Science Letters, v. 263, p. 180–191, https://doi.org/10.1016/j.epsl.2007.08.010.

Liu, L., Wang, C., Chen, D., Zhang, A., and Liou, J.G., 2009, Petrology and geochronology of HP-UHP rocks from the South Altyn Tagh, northwestern China: Journal of Asian Earth Sciences, v. 35, p. 232–244, https://doi.org/10.1016/j.jseaes.2008.10.007.

Liu, L., Wang, C., Cao, Y.T., Chen, D.L., Kang, L., Yang, W.Q., and Zhu, X.H., 2012, Geochronology of multi-stage metamorphic events: Constraints on episodic zircon growth from the UHP eclogite in the South Altyn, NW China: Lithos, v. 136, p. 10–26, https://doi.org/10.1016/j.lithos.2011.09.014.

Liu, Y.S., Gao, S., Hu, Z.C., Gao, C.G., Zong, K.Q., and Wang, D.B., 2010a, Continental and oceanic crust recycling-induced melt–peridotite interactions in the Trans–North China orogen: U-Pb dating, Hf isotopes and trace elements in zircons from mantle xenoliths: Journal of Petrology, v. 51, p. 537–571, https://doi.org/10.1093/petrology/egp082.

Liu, Y.S., Hu, Z.C., Zong, K.Q., Gao, C.G., Gao, S., Xu, J., and Chen, H.H., 2010b, Reappraisal and refinement of zircon U-Pb isotope and trace element analyses by LA-ICP-MS: Chinese Science Bulletin, v. 55, p. 1535–1546, https://doi.org/10.1007/s11434-010-3052-4.

Loucks, R.R., 1990, Discrimination from ophiolitic and nonophiolitic mafic-ultramafic allochthons in orogenic belts by the Al/Ti ratios in clinopyroxene: Geology, v. 18, p. 346–349, https://doi.org/10.1130/0091-7613(1990)018<0346:DOOFNU>2.3.CO;2.

Ludwig, K.R., 1999, Using Isoplot/EX, Version 2: A Geochronological Toolkit for Microsoft Excel: Berkeley Geochronology Center Special Publication 1a, 47 p.

Lugmair, G.W., and Harti, K., 1978, Lunar initial $^{143}Nd/^{144}Nd$: differential evolution of the lunar crust and mantle: Earth and Planetary Science Letters, v. 39, p. 349–357, https://doi.org/10.1016/0012-821X(78)90021-3.

Meng, F.C., Zhang, J.X., Yu, S.Y., and Chen, S.Y., 2010, The early Paleozoic pillow basalt in northern Altyn, western China and its tectonic implications: Acta Geologica Sinica, v. 84, p. 981–990 (in Chinese with English abstract).

Meng, L.T., Chen, B.L., Zhao, N.N., Wu, Y., Zhang, W.G., He, J.T., Wang, B., and Han, M.M., 2017, The distribution, geochronology and geochemistry of early Paleozoic granitoid plutons in the North Altun orogenic belt, NW China: Implications for the petrogenesis and tectonic evolution: Lithos, v. 268–271, p. 399–417, https://doi.org/10.1016/j.lithos.2016.10.022.

Miyashiro, A., 1974, Volcanic rock series in island arc and active continental margins: American Journal of Science, v. 274, p. 321–355, https://doi.org/10.2475/ajs.274.4.321.

Nakakuki, T., and Mura, E., 2013, Dynamics of slab rollback and induced back-arc basin formation: Earth and Planetary Science Letters, v. 361, p. 287–297, https://doi.org/10.1016/j.epsl.2012.10.031.

Ni, K., Wu, B., and Ye, X.T., 2017, Zircon LA-ICP-MS U-Pb dating of the rhyolite of the Lapeiquan Formation in North Altun Tagh, Xinjiang, and its implications: East China Geology, v. 3, p. 168–174 [in Chinese with English abstract].

Niu, H.C., Sato, H., Zhang, H.X., Ito, J., Yu, X.Y., Nagao, T., Terada, K., and Zhang, Q., 2006, Juxtaposition of adakite, boninite, high-$TiO_2$ and low-$TiO_2$ basalts in the Devonian southern Altay, Xinjiang, NW China: Journal of Asian Earth Sciences, v. 28, p. 439–456, https://doi.org/10.1016/j.jseaes.2005.11.010.

Pearce, J.A., 2014, Immobile element fingerprinting of ophiolites: Elements, v. 10, p. 101–108, https://doi.org/10.2113/gselements.10.2.101.

Pearce, J.A., and Peate, D.W., 1995, Tectonic implications of the composition of volcanic arc magmas: Annual Review of Earth and Planetary Sciences, v. 23, p. 251–285, https://doi.org/10.1146/annurev.ea.23.050195.001343.

Pearce, J.A., Stern, J.R., Bloomer, S.H., and Fryer, P., 2005, Geochemical mapping of the Mariana arc-basin system: Implications for the nature and distribution of subduction components: Geochemistry Geophysics Geosystems, v. 6, Q07006, https://doi.org/10.1029/2004GC000895.

Plank, T., and Langmuir, C.H., 1998, The chemical composition of subducting sediment and its consequences for the crust and mantle: Chemical Geology, v. 145, p. 325–394, https://doi.org/10.1016/S0009-2541(97)00150-2.

Qi, L., Hu, J., and Gregoire, D.C., 2000, Determination of trace elements in granites by inductively coupled plasma mass spectrometry: Talanta, v. 51, p. 507–513, https://doi.org/10.1016/S0039-9140(99)00318-5.

Qi, W.X., Ma, Y.Z., Wang, R., Wei, X.C., and Jiang, J.Y., 2008, The geological characteristics of Baba iron deposit, northern margin area of Altun Mountains, and its criteria for prospecting and genesis: Xinjiang Geology, v. 26, p. 253–257 [in Chinese with English abstract].

Qi, X.X., Wu, C.L., and Li, H.B., 2005a, Zircon SHRIMP U-Pb ages of Kazisayi granite in the northern Altun Tagh Mountains and its significance: Acta Petrologica Sinica, v. 21, p. 859–866 [in Chinese with English abstract].

Qi, X.X., Li, H.B., Wu, C.L., Yang, J.S., Zhang, J.X., Meng, F.C., Shi, R.D., and Chen, S.Y., 2005b, SHRIMP U-Pb zircon dating for Qiashikansayi granodiorite, the northern Altyn Tagh Mountains and its geological implications: Chinese Science Bulletin, v. 50, p. 440–445.

Qian, X., Wang, Y., Srithai, B., Feng, Q., Zhang, Y., Zi, J.W., and He, H., 2017, Geochronological and geochemical constraints on the intermediate-acid volcanic rocks along the Chiang Khong–Lampang-Tak igneous zone in NW Thailand and their tectonic implications: Gondwana Research, v. 45, p. 87–99, https://doi.org/10.1016/j.gr.2016.12.011.

Qin, J.F., Lai, S.C., Grapes, R., Diwu, C.R., Ju, Y.J., and Li, Y.F., 2010, Origin of Late Triassic high-Mg adakitic granitoid rocks from the Dongjiangkou area, Qinling orogen, central China: Implications for subduction of continental crust: Lithos, v. 120, p. 347–367, https://doi.org/10.1016/j.lithos.2010.08.022.

Rudnick, R.L., and Gao, S., 2003, Composition of the continental crust, *in* Holland, H.D., and Turekian, K.K., eds., Treatise on Geochemistry, Volume 3: The Mantle and the Core: Oxford, UK, Elsevier, p. 1–64.

Saunders, A.D., Norry, M.J., and Tarney, J., 1991, Fluid influence on the trace element compositions of subduction zone magmas: Philosophical Transactions of the Royal Society of London, v. 335, p. 377–392, https://doi.org/10.1098/rsta.1991.0053.

Shellnutt, J.G., and Zellmer, G.F., 2010, High-Mg andesite genesis by upper crustal differentiation: Journal of the Geological Society [London], v. 167, p. 1081–1088, https://doi.org/10.1144/0016-76492010-070.

Shimoda, G., Tatsumi, Y., Nohda, S., Ishizaka, K., and Jahn, B.M., 1998, Setouchi high-Mg andesites revisited: Geochemical evidence for melting of subducting sediments: Earth and Planetary Science Letters, v. 160, no. 3–4, p. 479–492, https://doi.org/10.1016/S0012-821X(98)00105-8.

Sisson, V.B., Pavlis, T.L., Roeske, S.M., and Thorkelson, D.J., 2003, Introduction: An overview of ridge-trench interaction in modern and ancient settings, *in* Sisson, V.B., Roeske, S.M., and Pavlis, T.L., eds., Geology of a Transpressional Orogen Developed During Ridge–Trench Interaction along the North Pacific Margin: Geological Society of America Special Paper 371, p. 1–18, https://doi.org/10.1130/0-8137-2371-X.1.

Snoke, A.W., Quick, J.E., and Bowman, H.R., 1981, Bear Mountain igneous complex, Klamath Mountains, California: An ultrabasic to silicic calc-alkaline suite: Journal of Petrology, v. 22, p. 501–552, https://doi.org/10.1093/petrology/22.4.501.

Sobel, E.R., and Arnaud, N., 1999, A possible middle Paleozoic suture in the Altyn Tagh, NW China: Tectonics, v. 18, p. 64–74, https://doi.org/10.1029/1998TC900023.

Stern, R.J., 2002, Subduction zones: Reviews of Geophysics, v. 40, p. 3-1–3-38, https://doi.org/10.1029/2001RG000108

Straub, S.M., Gomez-Tuena, A., Stuart, F.M., Zellmer, G.F., Espinasa-Perena, R., Cai, Y., and Iizuka, Y., 2011, Formation of hybrid arc andesites beneath thick continental crust: Earth and Planetary Science Letters, v. 303, p. 337–347, https://doi.org/10.1016/j.epsl.2011.01.013.

Streck, M.J., Leeman, W.P., and Chesley, J., 2007, High-magnesian andesite from Mount Shasta: A product of magma mixing and contamination, not a primitive mantle melt: Geology, v. 35, p. 351–354, https://doi.org/10.1130/G23286A.1.

Sun, J.M., Ma, Z.P., Tang, Z., and Li, X.M., 2012, Zircon LA-ICP-MS dating of the Yumuquan magma mixing granite in the southern Altun Tagh and its tectonic significance: Acta Geologica Sinica, v. 86, p. 247–257 [in Chinese with English abstract].

Sun, M., Long, X.P., Cai, K.D., Jiang, Y.D., Wang, B.Y., Yuan, C., Zhao, G.C., Xiao, W.J., and Wu, F.Y., 2009, Early Paleozoic ridge subduction in the Chinese Altai: Insight from the abrupt change in zircon Hf isotopic compositions: Science in China, ser. D, Earth Sciences, v. 52, p. 1345–1358, https://doi.org/10.1007/s11430-009-0110-3.

Sun, S.S., and McDonough, W.F., 1989, Chemical and isotopic systematics of ocean basalts: Implications for mantle composition and process, *in* Saunders, A.D., and Norry, M.J., eds., Magmatism in the Ocean Basins: Geological Society, London, Special Publication 42, p. 313–345, https://doi.org/10.1144/gsl.sp.1989.042.01.19.

Tang, G.J., and Wang, Q., 2010, High-Mg andesites and their geodynamic implications: Acta Petrologica Sinica, v. 26, p. 2495–2512 [in Chinese with English abstract].

Tang, Y.J., Zhang, H.F., and Ying, J.F., 2006, Asthenosphere–lithospheric mantle interaction in an extensional regime: Implication from the geochemistry of Cenozoic basalts from Taihang Mountains, North China craton: Chemical Geology, v. 233, p. 309–327, https://doi.org/10.1016/j.chemgeo.2006.03.013.

Tatsumi, Y., 1981, Melting experiments on a high-magnesian andesite: Earth and Planetary Science Letters, v. 54, p. 357–365, https://doi.org/10.1016/0012-821X(81)90017-0.

Tatsumi, Y., 2001, Geochemical modeling of partial melting of subducting sediments and subsequent melt–mantle interaction: Generation of high-Mg andesites in the Setouchi volcanic belt, southwest Japan: Geology, v. 29, p. 323–326, https://doi.org/10.1130/0091-7613(2001)029<0323:GMOPMO>2.0.CO;2.

Tatsumi, Y., and Eggins, S., 1995, Subduction Zone Magmatism: Cambridge, UK, Blackwell, 211 p.

Tatsumi, Y., and Hanyu, T., 2003, Geochemical modeling of dehydration and partial melting of subducting lithosphere: Toward a comprehensive understanding of high-Mg andesite formation in the Setouchi volcanic belt, SW Japan: Geochemistry Geophysics Geosystems, v. 4, 1081, https://doi.org/10.1029/2003GC000530.

Teng, L.S., Lee, C., Tsai, Y., and Hsiao, L.Y., 2000, Slab breakoff as a mechanism for flipping of subduction polarity in Taiwan: Geology, v. 28, p. 155–158, https://doi.org/10.1130/0091-7613(2000)28<155:SBAAMF>2.0.CO;2.

Tsuchiya, N., Suzuki, S., Kimura, J.I., and Kagami, H., 2005, Evidence for slab melt/mantle reaction: Petrogenesis of Early Cretaceous and Eocene high-Mg andesites from the Kitakami Mountains, Japan: Lithos, v. 79, p. 179–206, https://doi.org/10.1016/j.lithos.2004.04.053.

Turner, S., Hawkesworth, C., Rogers, N., Bartlett, J., Worthington, T., Hergt, J., Pearce, J., and Smith, I., 1997, $^{238}U$-$^{230}Th$ disequilibrium, magma petrogenesis, and flux rates beneath the depleted Tonga-Kermadec island arc: Geochimica et Cosmochimica Acta, v. 61, p. 4855–4884, https://doi.org/10.1016/S0016-7037(97)00281-0.

van Hunen, J., and Allen, M.B., 2011, Continental collision and slab break-off: A comparison of 3-D numerical models with observations: Earth and Planetary Science Letters, v. 302, p. 27–37, https://doi.org/10.1016/j.epsl.2010.11.035.

Wang, Q., Zhao, Z.H., Xu, J.F., Wyman, D.A., Xiong, X.L., Zi, F., and Bai, Z.H., 2006, Carboniferous adakite–high-Mg andesite–Nb-enriched basaltic rock suites in the Northern Tianshan area: Implications for Phanerozoic crustal growth in the Central Asia orogenic belt and Cu-Au mineralization: Acta Petrologica Sinica, v. 22, p. 11–30 [in Chinese with English abstract].

Wang, Q., Wyman, D.A., Xu, J., Dong, Y., Vasconcelos, P., Pearsone, N., Wang, Y., Dong, H., Li, C., Yu, Y., Zhu, T., Feng, X., Zhang, Q., Zi, F., and Chu, Z., 2008, Eocene melting of subducting continental crust and early uplifting of central Tibet: Evidence from central-western Qiangtang high-K calc-alkaline andesites, dacites and rhyolites: Earth and Planetary Science Letters, v. 272, p. 158–171, https://doi.org/10.1016/j.epsl.2008.04.034.

Wang, Q., Li, Z.X., Chung, S.L., Wyman, D.A., Sun, Y.L., Zhao, Z.H., Zhu, Y.T., and Qiu, H.N., 2011, Late Triassic high-Mg andesite/dacite suites from northern Hohxil, North Tibet: Geochronology, geochemical characteristics, petrogenetic processes and tectonic implications: Lithos, v. 126, p. 54–67, https://doi.org/10.1016/j.lithos.2011.06.002.

Wang, X.R., Gao, S., Liu, X.M., Yuan, H.L., Hu, Z.C., Zhang, H., and Wang, X.C., 2006, Geochemistry of high-Mg andesites from the Early Cretaceous Yixian Formation, western Liaoning: Implications for lower crustal delamination and Sr/Y variations: Science in China, ser. D, Earth Sciences, v. 49, p. 904–914, https://doi.org/10.1007/s11430-006-2016-7.

White, W.M., and Duncan, R.A., 1996, Geochemistry and geochronology of the Society Island: New evidence from deep mantle recycling, *in* Basu, A., and Hart, S.R., eds., Earth Processes: Reading the Isotopic Code: American Geophysical Union Geophysical Monograph 95, p. 183–206, https://doi.org/10.1029/GM095p0183.

Williams, I.S., 1998, U-Th-Pb geochronology by ion microprobe: Reviews in Economic Geology, v. 7, p. 1–35.

Winchester, J.A., and Floyd, P.A., 1977, Geochemical discrimination of different magma series and their differentiation products using immobile elements: Chemical Geology, v. 20, p. 325–343, https://doi.org/10.1016/0009-2541(77)90057-2.

Windley, B.F., Alexeiev, D., Xiao, W.J., Kroner, A., and Badarch, G., 2007, Tectonic models for accretion of the Central Asian orogenic belt: Journal of the Geological Society [London], v. 164, p. 31–47, https://doi.org/10.1144/0016-76492006-022.

Wood, B.J., and Turner, S.P., 2009, Origin of primitive high-Mg andesite: Constraints from natural examples and experiments: Earth and Planetary Science Letters, v. 283, p. 59–66, https://doi.org/10.1016/j.epsl.2009.03.032.

Wood, D.A., Joron, J.L., and Treuil, M., 1979, A re-appraisal of the use of trace elements to classify and discriminate between magma series erupted in different tectonic settings: Earth and Planetary Science Letters, v. 45, p. 326–336, https://doi.org/10.1016/0012-821X(79)90133-X.

Woodhead, J.D., Hergt, J.M., Davidson, J.P., and Eggins, S.M., 2001, Hafnium isotope evidence for 'conservative' element mobility during subduction zone processes: Earth and Planetary Science Letters, v. 192, p. 331–346, https://doi.org/10.1016/S0012-821X(01)00453-8.

Wu, C.L., Yao, S.Z., Zeng, L.S., Yang, J.S., Wooden, J.L., Chen, S.Y., and Mazadab, F.K., 2006, Bashikaogong-Shimierbulake granitic complex, North Altun, NW China: Geochemistry and zircon SHRIMP ages: Science China–Earth Sciences, v. 49, p. 1233–1251, https://doi.org/10.1007/s11430-006-2041-6.

Wu, C.L., Yang, J.S., Robinson, P.T., Wooden, J.L., Mazdab, F.K., Gao, Y., Wu, S., and Chen, Q., 2009, Geochemistry, age and tectonic significance of granitic rocks in North Altun, northwest China: Lithos, v. 113, p. 423–436, https://doi.org/10.1016/j.lithos.2009.05.009.

Wu, Y., Chen, Z.L., Chen, B.L., Wang, Y., Meng, L.T., He, J.T., Han, M.M., and Wang, B., 2016, Geochronological and geochemical characteristics of the deformed diorite from the North Altun brittle-ductile shear zone and its constraint on the early Paleozoic tectonic evolution of the North Altun Tagh: Acta Petrologica Sinica, v. 32, p. 555–570 [in Chinese with English abstract].

Xinjiang, BGMR, 1981, Geological Map of Shimiankuang, Xinjiang, China: Xinjiang, China, Xinjiang Bureau of Geology and Mineral Resources, scale 1:250,000 [in Chinese].

Xinjiang, BGMR., 2006, Geological Map of J46E006007 and J46E006008, Xinjiang, China: Xinjiang, China, Xinjiang Bureau of Geology and Mineral Resources, scale 1:50,000 [in Chinese].

Xu, J.F., Shinjo, R., Defant, M.J., Wang, Q.A., and Rapp, R.P., 2002, Origin of Mesozoic adakitic intrusive rocks in the Ningzhen area of east China: Partial melting of delaminated lower continental crust: Geology, v. 30, p. 1111–1114, https://doi.org/10.1130/0091-7613(2002)030<1111:OOMAIR>2.0.CO;2.

Xu, J.F., Castillo, P.R., Chen, F.R., Niu, H.C., Yu, X.Y., and Zhen, Z.P., 2003, Geochemistry of late Paleozoic mafic igneous rocks from the Kuerti area, Xinjiang, northwest China: Implications for backarc mantle evolution: Chemical Geology, v. 193, p. 137–154, https://doi.org/10.1016/S0009-2541(02)00265-6.

Xu, Y.G., Lan, J.B., Yang, Q.J., Huang, X.L., and Qiu, H.N., 2008, Eocene break-off of the Neo-Tethyan slab as inferred from intraplate-type mafic dykes in the Gaoligong orogenic belt, eastern Tibet: Chemical Geology, v. 255, p. 439–453, https://doi.org/10.1016/j.chemgeo.2008.07.016.

Xu, Z.Q., Yang, J.S., Zhang, J.X., Jiang, M., Li, H.B., and Cui, J.W., 1999, A comparison between the tectonic units on the two sides of the Altun sinistral strike-slip fault and the mechanism of lithospheric shearing: Acta Geologica Sinica, v. 73, p. 193–205 [in Chinese with English abstract].

Xu, Z.Q., Li, S.T., Zhang, J.X., Yang, J.S., He, B.Z., Li, H.B., Lin, C.S., and Cai, Z.H., 2011, Paleo-Asian and Tethyan tectonic systems with docking the Tarim block: Acta Petrologica Sinica, v. 27, p. 1–22 [in Chinese with English abstract].

Yan, H., Long, X., Wang, X.C., Li, J., Wang, Q., Yuan, C., and Sun, M., 2016, Middle Jurassic MORB-type gabbro, high-Mg diorite, calc-alkaline diorite and granodiorite in the Ando area, central Tibet: Evidence for a slab roll-back of the Bangong-Nujiang Ocean: Lithos, v. 264, p. 315–328, https://doi.org/10.1016/j.lithos.2016.09.002.

Yang, J.S., Shi, R.D., Wu, C.L., Su, D.C., Chen, S.Y., Wang, X.B., and Wooden, J.L., 2008, Petrology and SHRIMP age of the Hongliugou ophiolite at Milan, North Altun, at the northern margin of the Tibetan Plateau: Acta Petrologica Sinica, v. 24, p. 1567–1584 [in Chinese with English abstract].

Yang, S.H., and Zhou, M.F., 2009, Geochemistry of the similar to 430-Ma Jingbulake mafic-ultramafic intrusion in western Xinjiang, NW China: Implications for subduction related magmatism in the South Tianshan orogenic belt: Lithos, v. 113, p. 259–273, https://doi.org/10.1016/j.lithos.2009.07.005.

Ye, X.T., Zhang, C.L., Zou, H.B., Zhou, G., Yao, C.Y., and Dong, Y.G., 2015, Devonian Alaskan-type ultramafic-mafic intrusions and silicic igneous rocks along the southern Altai orogen: Implications on the Phanerozoic continental growth of the Altai orogen of the Central Asian orogenic belt: Journal of Asian Earth Sciences, v. 113, p. 75–89, https://doi.org/10.1016/j.jseaes.2014.08.008.

Yin, A., and Harrison, T.M., 2000, Geologic evolution of the Himalayan-Tibetan orogen: Annual Review of Earth and Planetary Sciences, v. 28, p. 211–280, https://doi.org/10.1146/annurev.earth.28.1.211.

Yogodzinski, G.M., Kay, R.W., Volynets, O.N., Koloskov, A.V., and Kay, S.M., 1995, Magnesian andesite in the western Aleutian Komandorsky region: Implications for slab melting and processes in the mantle wedge: Geological Society of America Bulletin, v. 107, p. 505–519, https://doi.org/10.1130/0016-7606(1995)107<0505:MAITWA>2.3.CO;2.

Zhang, C.L., Zou, H.B., Santosh, M., Ye, X.T., and Li, H.K., 2014, Is the Precambrian basement of the Tarim craton in NW China composed of discrete terranes: Precambrian Research, v. 254, p. 226–244, https://doi.org/10.1016/j.precamres.2014.08.006.

Zhang, J.X., and Meng, F.C., 2006, Lawsonite-bearing eclogites in the North Qilian and North Altun Tagh: Evidence for cold subduction of oceanic crust: Chinese Science Bulletin, v. 51, p. 1238–1244, https://doi.org/10.1007/s11434-006-1238-6.

Zhang, J.X., Mattinson, C.G., Meng, F.-C., and Wan, Y.S., 2005a, An early Palaeozoic HP/HT granulite-garnet peridotite association in the South Altun Tagh, NW China: *P-T* history and U-Pb geochronology: Journal of Metamorphic Geology, v. 23, p. 491–510, https://doi.org/10.1111/j.1525-1314.2005.00585.x.

Zhang, J.X., Meng, F.C., and Yang, J.S., 2005b, A new HP/LT metamorphic terrane in the northern Altun Tagh, western China: International Geology Review, v. 47, p. 371–386, https://doi.org/10.2747/0020-6814.47.4.371.

Zhang, J.X., Meng, F.C., Yu, S.Y., Chen, W., and Chen, S.Y., 2007, $^{40}Ar$-$^{39}Ar$ geochronology of high pressure/low temperature blueschist and eclogite in the North Altun Tagh and their tectonic implications: Geology in China, v. 34, p. 558–564 [in Chinese with English abstract].

Zhang, J.X., Meng, F.C., and Yu, S.Y., 2010, Two contrasting HP/LT and UHP metamorphic belts: Constraints on early Paleozoic orogeny in the Qilian-Altun orogen: Acta Petrologica Sinica, v. 26, p. 1967–1992 [in Chinese with English abstract].

Zhang, J.X., Yu, S.Y., Li, Y.S., Yu, X.X., Lin, Y.H., and Mao, X.H., 2015, Subduction, accretion and closure of the proto–Tethyan Ocean: Early Paleozoic accretion/collision orogeny in the Altun–Qilian–North Qaidam orogenic system: Acta Petrologica Sinica, v. 31, p. 3531–3554 [in Chinese with English abstract].

Zhang, J.X., Yu, S.Y., and Mattinson, C.G., 2017, Early Paleozoic polyphase metamorphism in northern Tibet, China: Gondwana Research, v. 41, p. 267–289, https://doi.org/10.1016/j.gr.2015.11.009.

Zhang, Y., Wang, Y., Fan, W., Zhang, A., and Ma, L., 2012, Geochronological and geochemical constraints on the metasomatised source for the Neoproterozoic (~825Ma) high-Mg volcanic rocks from the Cangshuipu area (Hunan Province) along the Jiangnan domain and their tectonic implications: Precambrian Research, v. 220–221, p. 139–157, https://doi.org/10.1016/j.precamres.2012.07.003.

Zhang, Z.C., Guo, Z.J., Feng, Z.S., and Li, J.F., 2010, SHRIMP U-Pb age of zircons from Suoerkuli rhyolite in the Altun Tagh Mountains and its geological significance: Acta Petrologica Sinica, v. 26, p. 597–606 [in Chinese with English abstract].

Zhu, D.C., Wang, Q., Zhao, Z.D., Chung, S.L., Cawood, P.A., Niu, Y., Liu, S.A., Wu, F.Y., and Mo, X.X., 2015, Magmatic record of India-Asia collision: Scientific Reports, v. 5, p. 14289, https://doi.org/10.1038/srep14289.

Zhu, W.G., Zhong, H., Li, X.H., He, D.F., Song, X.Y., Ren, T., Chen, Z.Q., Sun, H.S., and Liao, J.Q., 2010, The Early Jurassic mafic-ultramafic intrusion and A-type granite from northeastern Guangdong, SE China: Age, origin, and tectonic significance: Lithos, v. 119, p. 313–329, https://doi.org/10.1016/j.lithos.2010.07.005.

Zimmer, M., Kroner, A., Jochum, K.P., Reischmann, T., and Todt, W., 1995, The Gabal Gerf complex: A Precambrian N-MORB ophiolite in the Nubian Shield, NE Africa: Chemical Geology, v. 123, p. 29–51, https://doi.org/10.1016/0009-2541(95)00018-H.

Zindler, A., and Hart, S.R., 1986, Chemical geodynamics: Annual Review of Earth and Planetary Sciences, v. 14, p. 493–571, https://doi.org/10.1146/annurev.ea.14.050186.002425.

MANUSCRIPT RECEIVED 6 FEBRUARY 2018
REVISED MANUSCRIPT RECEIVED 20 JULY 2018
MANUSCRIPT ACCEPTED 6 SEPTEMBER 2018